



TU WIEN
DEPARTMENT OF
GEODESY AND
GEOINFORMATION

DIPLOMARBEIT

Evaluation of Commercial Off-the-Shelf GNSS Receivers for Nanosatellite Applications

zur Erlangung des akademischen Grades

Diplom-Ingenieur/in

ausgeführt am Department für

Geodäsie und Geoinformation

Forschungsbereich Höhere Geodäsie

der Technischen Universität Wien

unter Anleitung von

Ass.Prof. Dipl.-Ing. Dr.techn. Gregor Möller

und

Univ.Ass. Dipl.-Ing. Gerald Bauer

durch

Fiona-Evita Tschofen

Matrikelnummer: 11907046

Wien, im Dezember 2025

Unterschrift (Verfasser/in)

Unterschrift (Betreuer/in)

Eidesstattliche Erklärung

Ich erkläre an Eides statt, dass die vorliegende Arbeit nach den anerkannten Grundsätzen für wissenschaftliche Abhandlungen von mir selbstständig erstellt wurde. Alle verwendeten Hilfsmittel, insbesondere die zugrunde gelegte Literatur, sind in dieser Arbeit genannt und aufgelistet. Die aus den Quellen wörtlich entnommenen Stellen, sind als solche kenntlich gemacht.

Das Thema dieser Arbeit wurde von mir bisher weder im In- noch Ausland einer Beurteilerin/einem Beurteiler zur Begutachtung in irgendeiner Form als Prüfungsarbeit vorgelegt. Diese Arbeit stimmt mit der von den Begutachterinnen/Begutachtern beurteilten Arbeit überein.

Wien, im Dezember 2025

Kurzfassung

Diese Arbeit untersucht die Leistungsfähigkeit kostengünstiger GNSS (Global Navigation Satellite Systems)-Empfänger für den Einsatz auf Nanosatelliten im Low Earth Orbit (LEO). Zu diesem Zweck wurden GPS-Signale mit dem *XPLORA*-Simulator der Firma OHB Austria unter realitätsnahen orbitalen Bedingungen erzeugt. Die simulierten Szenarien umfassten statische und kinematische Flugphasen eines Astrocaster CubeSat Nanosatelliten, wobei Trajektorienfehler des Simulators durch eine externe Spline-Interpolation korrigiert wurden. Zwei kommerziell verfügbare Empfänger (u-blox ZED-F9P and "RAKON GNSS Development Kit for Nanosatellite Applications") wurden hinsichtlich ihrer Signalverfolgung, Beobachtungsqualität und Positionsgenauigkeit analysiert. Die gewonnenen RINEX-Daten wurden mit präzisen Ephemeriden in der Precise Point Positioning (PPP)-Software *raPPPid* verarbeitet, wobei sowohl Code- als auch kombinierte Code- und Phasenmessungen berücksichtigt wurden.

Die Ergebnisse zeigen, dass beide Empfänger grundsätzlich in der Lage sind, zuverlässige GNSS-Beobachtungen unter LEO-ähnlichen Bedingungen zu liefern. Allerdings führt eine reduzierte Eingangssignalstärke (bis -100 dBm) zu einer deutlich geringeren Signalqualität, häufigeren Tracking-Unterbrechungen, verlängerten Akquisitionszeiten sowie einer verringerten Anzahl beobachteter Satelliten. Für Code-only-Lösungen werden Genauigkeiten im Meterbereich erreicht, während die Kombination von Code- und Phasenbeobachtungen zu Genauigkeiten im Dezimeterbereich und, für statische Szenarien, im Zentimeterbereich führt. Kinematische Höhenlösungen weisen einen systematischen Offset auf, der vermutlich auf simulatorbedingte Effekte zurückzuführen ist und die tatsächliche Leistung der Empfänger im Orbit vermutlich unterschätzt.

Insgesamt bestätigen die Ergebnisse das Potenzial kostengünstiger GNSS-Technologie für den Einsatz auf LEO-Nanosatelliten, zeigen jedoch zugleich die Notwendigkeit einer sorgfältigen Empfängerkonfiguration und einer Verbesserung der Simulationsumgebung, insbesondere bezüglich hochdynamischer Szenarien.

Abstract

This study evaluates the performance of low-cost GNSS (Global Navigation Satellite Systems) receivers for use on nanosatellites operating in Low Earth Orbit (LEO). GPS signals were generated under realistic orbital conditions using the OHB Austria *XPLORA* simulator. The simulated scenarios include both static and highly kinematic phases based on an Astrocaster CubeSat nanosatellite trajectory, for which interpolation artefacts in the simulator were corrected via external spline interpolation. Two commercial receivers (u-blox ZED-F9P and "RAKON GNSS Development Kit for Nanosatellite Applications") were assessed with regard to signal tracking capability, observation quality, and achievable positioning accuracy. All data were converted to RINEX format and processed using the precise point positioning (PPP) software *raPPPid*, applying consistent modelling for both code-only and combined code-and-carrier-phase solutions.

The results indicate that both receivers can maintain stable GNSS tracking under LEO-like conditions, although reduced input power levels (down to -100 dBm) significantly degrade signal quality, increase the number of tracking interruptions, and prolong acquisition times. Code-based positioning yields metre-level accuracy, while the inclusion of carrier-phase observations enables decimetre-level precision and, in static cases, centimetre-level results. However, a pronounced systematic offset appears in the kinematic height solutions, which is most likely introduced by the simulation environment rather than by the receivers themselves, suggesting that real on-orbit performance may be superior to the results obtained with the current simulator configuration.

Overall, the findings confirm the feasibility of employing low-cost GNSS receivers on LEO nanosatellites, provided that receiver configurations are adapted to the high-dynamics orbital environment.

Contents

Kurzfassung	II
Abstract	III
List of Abbreviations	VI
1 Introduction	1
1.1 State of the Art	1
2 Global Navigation Satellite Systems and Precise Point Positioning	3
2.1 Global Navigation Satellite Systems (GNSS)	3
2.1.1 Observation Modelling	3
2.1.2 Error Sources	4
2.1.3 Signal and Tracking	5
2.2 Absolute Positioning	6
2.2.1 Precise Point Positioning (PPP)	7
2.2.2 Kalman Filter	9
3 Methods	11
3.1 Simulation of GNSS Signals	11
3.2 Receivers Used in this Study	12
3.3 Measurement Setup	12
3.4 Data Collection	14
3.5 PPP with <i>raPPPid</i>	15
3.6 Further Processing and Analysis	18
4 Results	19
4.1 Tracking Analysis	19
4.1.1 Skyplot	20
4.1.2 Number of Observations	20
4.1.3 Observation Gaps	20
4.1.4 Number of Tracked Satellites	23
4.1.5 Time Delay to First Tracking	23
4.2 Signal Analysis	26
4.2.1 Distribution of C/N_0	26
4.2.2 Carrier-to-Noise Density Ratio	27
4.3 Position Solution with Code Observations	28
4.3.1 Static Receiver	28
4.3.2 Kinematic Receiver	30
4.4 Position Solution with Code and Phase Observations	32
4.4.1 Static Receiver	32

Contents

4.4.2 Kinematic Receiver	35
5 Discussion	39
5.1 Signal and Tracking	39
5.2 Position Solution	40
6 Conclusion	42
6.1 Summary and Answers to Research Questions	42
6.2 Limitations	42
6.3 Outlook on Future Work	42
List of Figures	43
List of Tables	45
References	46

List of Abbreviations

C/N₀ Carrier-to-Noise density ratio

DLL Delay Lock Loop

GEO Geostationary Orbit

GNSS Global Navigation Satellite Systems

GPS Global Positioning System

HEO High Earth Orbit

IGS International GNSS Service

LEO Low Earth Orbit

MEO Medium Earth Orbit

PLL Phase Lock Loop

POD Precision Orbit Determination

PPP Precise Point Positioning

PRN Pseudo-Random Noise Code

PVT Position, Velocity and Time

SNR Signal-to-Noise Ratio

1 Introduction

Nanosatellites in LEO (Low Earth Orbit) are subject to strict constraints regarding weight, volume, and power consumption. With the growing number of such satellites and decreasing launch costs, there is increasing interest in utilizing commercially available, low-cost GNSS (Global Navigation Satellite Systems) receivers for precise positioning. These devices, however, are typically developed for terrestrial applications, and their functionality in space has to be evaluated.

At TU Wien, the precise point positioning (PPP) software *raPPPid* has been developed to compute positions from GNSS observations, supporting both static and kinematic positioning on Earth. However, its ability to process highly kinematic data, such as from LEO satellites, is currently limited. To enable accurate positioning in space, the integration of a dynamic model into the extended Kalman filter and optimization of its parameters is necessary. The thesis aims to address the following research questions:

- How do commercial GNSS receivers perform in terms of satellite tracking, signal quality and position accuracy under simulated space conditions?
- Are the low-cost receivers suitable for precise orbit determination?
- How good are space-borne PPP results from *raPPPid*?

1.1 State of the Art

The growing maturity of spaceborne GNSS technology has enabled highly accurate real-time navigation for a wide range of LEO missions. Demonstrating this progress, Montenbruck et al. (2021) have shown that real-time GNSS-based navigation with three-dimensional position errors at the level of approximately 10 cm is feasible for operational missions such as Sentinel-6.

Further advances were reported by Capuano et al. (2013), who reviewed the use of GNSS for LEO spacecraft orbit and attitude determination, proximity operations, formation flying, and timing synchronisation. Their analysis covered the expected performance of GPS and Galileo for missions in MEO (Medium Earth Orbit), GEO (Geostationary Orbit), HEO (High Earth Orbit), and even lunar transfer scenarios. Simulation results confirmed that GNSS-based navigation is viable across these regimes. Particular emphasis was placed on the minimum signal power levels required for acquisition and tracking, ranging from roughly -120.8 dBm to -162.7 dBm depending on the orbital geometry and the particular set of GNSS constellations employed. They further highlighted the need to cope with Doppler shifts between 15 kHz and 55 kHz and demonstrated the clear advantages of multi-constellation receivers.

In the context of precision orbit determination (POD), Allahviridi-Zadeh et al. (2022) showed that post-processed POD yields orbit solutions with accuracies of several centimetres. However, they noted that purely kinematic solutions degrade in epochs affected by data outages (a common issue for power-limited CubeSats). For such platforms, reduced-dynamic POD provides a more robust alternative, while simplified force models may be adopted to enable onboard implementation.

A generic POD strategy capable of accommodating manoeuvres for LEO satellites equipped with high-performance GNSS receivers was introduced by Mao et al. (2023). Their results demonstrate absolute orbit accuracies at the centimetre level or better, underscoring the potential of advanced algorithms when high-quality GNSS measurements are available.

More recently, Montenbruck et al. (2025) reported three-dimensional RMS orbit errors of about 9 cm for Sentinel-6A with respect to a precise reference trajectory, further illustrating the present capability of spaceborne GNSS for high-accuracy orbit determination.

Studies of low-cost receivers have also shown considerable progress. Hohensinn et al. (2022) examined the performance of the u-blox ZED-F9P in the context of real-time PPP and high-rate dynamic applications such as seismological monitoring. Using static data processed under kinematic assumptions, they demonstrated that centimetre-level precision is achievable, indicating that even low-cost hardware can deliver precise results. Müller et al. (2024) analysed more than a year of navigation data from eight Astrocast CubeSats (using u-blox NEO-M8T receivers) and observed that position errors vary considerably over time and between satellites, ranging from a few meters up to several tens of meters. A positive radial offset of roughly 6–15 m between measured and simulated positions was attributed to ionospheric refraction.

Overall, the literature indicates that state-of-the-art GNSS processing enables sub-decimetre orbit determination for well-instrumented LEO missions, while recent findings suggest that low-cost receivers, when coupled with appropriate algorithms, may offer competitive performance for nanosatellite applications. Some studies make use of the widely available u-blox F9P, yet no published work to date investigates the performance of a rakon GNSS receiver in LEO, leaving its capabilities and limitations entirely unassessed. This motivates a detailed assessment of low-cost GNSS technology (specifically of rakon receivers) tailored to the constraints and operational environments of LEO nanosatellites.

2 Global Navigation Satellite Systems and Precise Point Positioning

2.1 Global Navigation Satellite Systems (GNSS)

GNSS is used to determine positions and is fundamentally based on measuring the arrival time of satellite signals. For position calculation, the system evaluates differences in time or phase between the received signal and a reference signal generated within the receiver.

Modern GNSS receivers determine satellite ranges using code and carrier-phase measurements. Because GNSS relies on one-way signal transmission between independent satellite and receiver clocks, any clock mismatch directly affects the derived distances. Additional systematic and random effects further influence the measurements, so the resulting ranges are referred to as pseudoranges (Hofmann-Wellenhof et al., 2008).

This work uses only the GPS L1 frequency, the primary legacy signal, providing robust code and carrier-phase measurements. Focusing on a single frequency simplifies processing while retaining the core principles of GNSS positioning and precise point positioning.

2.1.1 Observation Modelling

The receiver determines the temporal difference between the transmission and reception of a satellite signal using a correlation procedure. Multiplying this measured time offset by the speed of light yields the code-based observable, as shown in Equation 2.1 (adapted from Hauschild (2017)).

Besides code, the receiver also tracks the carrier phase by comparing the incoming signal with an internal reference, compensating for Doppler shifts and determining the phase offset. Converting the tracked phase (in cycles) to metres using the carrier wavelength yields observations that are typically two orders of magnitude more precise than code measurements (Hauschild, 2017).

A major distinction between the code and carrier phase measurements is the presence of an integer ambiguity term in the latter. Exploiting the superior precision of phase observations requires estimating this ambiguity, i.e. determining the number of full carrier wavelengths along the signal path.

The fundamental GNSS observation equations describe the relationship between the measured quantities (code and carrier phase) and the true geometric distance between satellite and receiver, incorporating multiple correction terms accounting for physical and system-related effects.

The pseudorange equation for code observations from Hauschild (2017) adapted to simulated space conditions and neglecting atmospheric effects, is given in Equation 2.1:

$$P = \rho + c(\Delta t_{\text{rec}} - \Delta t_{\text{sat}}) + \Delta_{\text{rel}} + B_{\text{rec}} - B_{\text{sat}} + \varepsilon \quad (2.1)$$

P is the measured pseudorange, ρ the true geometric distance between receiver and satellite, c the speed of light in vacuum, Δt_{rec} the receiver clock offset, Δt_{sat} the satellite clock offset, Δ_{rel} the relativistic correction, B_{rec} and B_{sat} hardware delays of receiver and satellite and ε are residual unmodelled errors.

The corresponding equation for the carrier phase observable (Hauschild, 2017), assuming simulated conditions without an atmosphere, extends the pseudorange equation by including wavelength-dependent phase terms and the integer ambiguity, as shown in Equation 2.2:

$$\Phi = \rho + c(\Delta t_{\text{rec}} - \Delta t_{\text{sat}}) + \Delta_{\text{rel}} - \lambda(N + b_{\text{rec}} - b_{\text{sat}}) + \varepsilon \quad (2.2)$$

where Φ describes the measured carrier phase observable, λ the carrier wavelength, N the integer carrier-phase ambiguity and b_{rec} and b_{sat} are the hardware induced phase biases of receiver and satellite. All other symbols are defined in Equation 2.1.

In addition to code and carrier phase measurements, the Doppler shift of the received signal is also observed. The Doppler effect refers to the change in the signal frequency caused by the relative motion between the satellite and the receiver. This observable is particularly valuable in applications involving kinematic PPP and for detecting cycle slips. The raw Doppler measurement is directly proportional to the radial component of the relative velocity, making it well suited for real-time velocity estimation and therefore highly relevant for navigation purposes. For more information, see for example Kaplan and Hegarty (2006).

2.1.2 Error Sources

GNSS measurements are subject to a number of systematic and stochastic error sources. For ground-based users, significant contributions arise from multipath effects and atmospheric influences, particularly due to the troposphere and ionosphere. However, in the context of this thesis, attention is restricted to error sources relevant to spaceborne GNSS applications.

One major class of errors stems from inaccuracies in the receiver and satellite clocks. Applying differences between measurements can mitigate these effects: forming differences between receivers removes satellite-dependent biases, while differencing between satellites eliminates receiver-dependent ones. Consequently, double-differenced pseudorange observations are largely free from these systematic clock errors.

2.1.3 Signal and Tracking

Signal acquisition provides coarse initial estimates of the code phase and the Doppler frequency, effectively locating the satellite signal within the receiver search space through a two-dimensional search in code phase and frequency using correlation. Once these first estimates have been obtained, the tracking loops take over and refine them continuously during operation. GNSS receivers employ two main tracking control loops within the correlator to maintain lock: the code tracking loop and the carrier tracking loop. The following description of the tracking-loop mechanisms is based on the detailed discussion provided in Pratap and Per (2006).

For code tracking, most receivers use a Delay Lock Loop (DLL). In a DLL, the incoming signal is correlated with two replica signals generated internally by the receiver: one slightly advanced and one slightly delayed in time. By comparing the two correlation outputs, the DLL determines the deviation of the received code phase and adjusts the replica code accordingly. This enables the receiver to maintain lock on the incoming code. Adjusting the DLL bandwidth directly affects tracking performance: larger bandwidths improve responsiveness under high dynamics but increase measurement noise, whereas smaller bandwidths reduce noise at the cost of robustness (Borre et al., 2006).

Carrier tracking is performed by a Phase Lock Loop (PLL). In addition to keeping the locally generated carrier aligned with the incoming carrier signal, the PLL also provides an estimate of the carrier phase. The noise-equivalent bandwidth of the PLL must be chosen to balance dynamic performance with noise sensitivity. Environments involving high dynamics require a larger loop bandwidth, whereas low-dynamic conditions permit a narrower bandwidth. For example, with a signal-to-noise ratio of 30 dBHz and a maximum acceleration of approximately 1 g, an optimal bandwidth is slightly above 20 Hz. If the maximum acceleration is lower, the optimal loop bandwidth also decreases. Narrow bandwidths can lead to insufficient response under rapid motion, while excessively wide bandwidths degrade noise performance.

Hofmann-Wellenhof et al. (1997) describe how phase measurements are ultimately performed within the tracking loops, which may employ either of two general approaches: (1) code correlation techniques, which require knowledge of the satellite PRN (Pseudo-Random Noise) code, or (2) codeless techniques, which operate without direct knowledge of the code. In both cases, the objective is to reconstruct the unmodulated carrier signal, from which the carrier-phase observations are derived.

The same authors then explain code correlation, which is employed in most receivers. This method provides access to the navigation message, the satellite clock information and the unmodulated carrier. The process involves generating a reference carrier in the receiver,

which is modulated with a replica of the satellite's PRN code. This reference signal is then correlated with the incoming signal. The correlation process shifts the locally generated signal in time until the maximum correlation is achieved, corresponding to the signal travel time (neglecting clock offsets) from the satellite antenna to the receiver phase centre. Afterwards the PRN code and the navigation message can be removed. The resulting signal consists of the Doppler-shifted carrier, on which precise phase measurements can be carried out.

The transmission power of the GNSS signal plays a significant role in the quality of signal reception. As noted by Yao and Lu (2021), the received signal strength is influenced by several factors including the transmission process, propagation effects, antenna characteristics and receiver design. Increasing the transmitted power improves the signal-to-noise ratio (SNR), enhancing signal clarity and reducing the effects of interference. A higher SNR means a stronger signal relative to background noise, which improves the reliability of navigation and positioning. In practice, GNSS receivers typically monitor this quantity as the carrier-to-noise density ratio (C/N_0), which provides a direct measure of signal quality at the tracking stage.

However, increasing transmission power is not without disadvantage. A stronger signal requires greater output power from the satellite transmitter or additional antenna gain, both of which increase system cost and technical complexity.

2.2 Absolute Positioning

Absolute positioning refers to the determination of a receiver's position in a global reference frame using measurements from one receiver alone (Kaplan and Hegarty, 2006). Typically, the receiver estimates its position by solving the pseudorange equations. This approach provides standalone position solutions without requiring a reference station, but is generally limited in accuracy by satellite geometry, receiver noise (and on earth by atmospheric delays). The pseudorange derived from code measurements (cf. Formula 2.1) is affected by both the satellite clock error and the receiver clock offset with respect to GNSS time. Each satellite introduces an individual clock bias. The satellite clock parameters are broadcast to the user through the navigation message.

Hofmann-Wellenhof et al. (1997) describe three methods for absolute positioning:

- 1. Point positioning with code ranges** At a single epoch, the system contains four unknown parameters: the three receiver coordinates and the receiver clock bias. If four satellites are tracked simultaneously, these quantities can be directly determined. Since each epoch can be treated independently, both the position and the clock offset at that epoch can

be estimated without relying on measurements from other epochs. Consequently, receiver motion does not interfere with the estimation process. In purely static scenarios where the receiver remains fixed over the observation interval, the strict requirement of observing four satellites simultaneously may be relaxed, because positional constancy across epochs provides additional constraints.

2. Point positioning with carrier phases Positioning using carrier-phase measurements exploits the phase of the received satellite signals to achieve positioning accuracies at the centimetre level. Unlike code-based pseudorange measurements, which are limited to meter-level precision, carrier-phase observations provide much finer resolution because they track the signal at the scale of its wavelength (e.g., ~ 19 cm for L1).

3. Point positioning with Doppler data In this method, the corresponding observation equations contain only the receiver clock drift rather than the full receiver clock offset, because Doppler measurements reflect frequency changes over time rather than absolute timing differences.

According to Kaplan and Hegarty (2006) the nonlinear observation equations arising from code-only or combined code and phase data may be addressed using one of several computational schemes: closed-form approaches, iterative algorithms based on linearisation, or Kalman filtering, which facilitates improved PVT (position, velocity and time) estimation by optimally exploiting the temporal structure of the measurement sequence.

2.2.1 Precise Point Positioning (PPP)

Precise Point Positioning (developed by Malys and Jensen (1990), Héroux and Kouba (1995) and Zumberge et al. (1997)) denotes a high-accuracy positioning strategy that enables centimetre to millimetre-level coordinates using observations from a single GNSS receiver. In contrast to classical double-difference techniques, where many error terms cancel naturally, PPP must explicitly correct a wide range of error sources in the undifferenced carrier-phase and code measurements (Pratap and Per, 2006). Owing to this, PPP requires highly refined observation models and external information of superior quality.

PPP is founded on undifferenced, dual- or multi-frequency carrier-phase observations and the corresponding pseudorange measurements (Savchuk et al., 2020). Two principal categories of information contribute to the PPP solution: the raw observables collected by the receiver and the precise satellite products (clock and orbit information), also known as ephemerides, generated by dedicated analysis centres. These external products generally replace the broadcast ephemerides; for example, solutions offered by the International GNSS Service (IGS) provide the high-fidelity satellite states required for PPP.

PPP achieves its high accuracy by exploiting the precision of the carrier-phase observable. Since only the fractional part of the phase is directly observed, the unknown full-cycle count introduces the integer ambiguity, which must be estimated as an additional parameter, typically within a Kalman filter.

In addition to estimating the receiver position in Earth-Centred Earth-Fixed (ECEF) coordinates and the receiver clock offset, PPP also requires the estimation of satellite-specific code-phase biases and the carrier-phase ambiguities themselves (Kaplan and Hegarty, 2006). The authors further state that these parameters are updated recursively using a sequential estimator, most commonly a Kalman filter.

Because the predicted measurements from the observation model can never perfectly match the observations recorded by the receiver, a difference between the two always remains. These remaining differences after parameter estimation are referred to as residuals. They indicate how well the observation model represents reality: small residuals suggest a good fit, whereas large residuals point to unmodelled effects, measurement errors, or issues such as undetected cycle slips. More accurate satellite products generally reduce residuals and improve the solution. Residuals are computed for both code and carrier-phase observations.

Achieving decimetre- or centimetre-level accuracy further necessitates modelling several error sources that are negligible in stand-alone or conventional differential GNSS. In this work, only the following error sources are considered, as it focuses on simulating space conditions:

Phase Wind-Up GNSS satellites transmit right-hand circularly polarised signals, produced by two perpendicular dipoles with a 90° phase offset, which causes the field vector to rotate. If either the satellite or the receiver antenna rotates about its boresight, the orientation between antenna and field changes, introducing an extra phase term known as phase wind-up. This effect arises naturally as satellites adjust their attitude in orbit. A full 360° rotation corresponds to roughly one carrier wavelength (about 20–25 cm). Further background is given in Pratap and Per (2006) and Glaner (2022), and the mathematical formulation is provided by Wu et al. (1993).

Cycle Slips Cycle slips are sudden breaks in the carrier-phase time series, typically caused by signal blockages, low SNR, or receiver processing issues (Hofmann-Wellenhof et al., 2008). As PPP depends on stable carrier-phase ambiguities, undetected slips can strongly degrade the solution, making reliable detection and correction essential. If fewer than four satellites are tracked during a slip, the affected ambiguities must be reinitialised.

Receiver Noise Although generally small in comparison, thermal noise in the receiver contributes to both phase and code observations.

Relativistic Effects Both special and general relativistic phenomena influence satellite clock rates, about which Hofmann-Wellenhof et al. (2008) provides detailed information. A first-order correction is implemented directly at the satellite by applying a frequency offset to the onboard clocks. A second correction, dependent on satellite velocity and gravitational potential along the orbit, must be applied by the user.

Although important in PPP applications on the Earth's surface, the following effects lie outside the scope of this study: antenna phase centre offsets and variations (PCOs and PCVs), geophysical site displacement models (solid Earth tides, pole tides, ocean loading, atmospheric loading), as well as tropospheric or ionospheric modelling.

Beyond precise positioning, PPP approaches are also employed in estimating atmospheric parameters (troposphere and ionosphere), and for high-precision time and frequency transfer between remote stations. Overviews of such applications are provided by Teunissen (2020) and Karabatić (2011).

2.2.2 Kalman Filter

In a dynamic (kinematic) setting, such as a moving vehicle or, in our case, a satellite, the quantities to be estimated are collected in a state vector. This vector evolves over time and its values at an epoch t can be forecast by means of the system's dynamic equations. Observations that contain information about the state are then used to refine these predictions. This recursive prediction–update mechanism constitutes the essence of the Kalman filter, introduced by Kalman (1960).

In PPP, the Kalman filter is the primary method for estimating time-dependent and slowly varying parameters. Each epoch's estimates provide prior information for the next, enabling continuous refinement. Owing to the non-linear PPP observation equations, an Extended Kalman Filter is usually applied (Glaner, 2022; Hofmann-Wellenhof et al., 2008). Further details are given in Hofmann-Wellenhof et al. (2008), Verhagen and Teunissen (2017) and Andrews and Grewal (2008).

The filter requires initial parameter estimates and corresponding covariance information. Following Glaner (2022), three computational stages are performed at each epoch:

1. Computation of the Gain Matrix The Kalman gain matrix \mathbf{G} determines the relative weighting of the new observations against the predicted state from previous epochs. It is obtained as

$$\mathbf{G} = \mathbf{Q}_{x,\text{pred}} \mathbf{A}^T (\mathbf{Q}_1 + \mathbf{A} \mathbf{Q}_{x,\text{pred}} \mathbf{A}^T)^{-1}, \quad (2.3)$$

where $\mathbf{Q}_{x,\text{pred}}$ is the predicted covariance matrix of the parameters, \mathbf{Q}_l denotes the covariance matrix of the observations, and \mathbf{A} is the design matrix representing the linearised functional model.

2. Parameter Adjustment The state vector (\mathbf{x}_{adj}) and its covariance ($\mathbf{Q}_{x,\text{adj}}$) are updated according to

$$\mathbf{x}_{\text{adj}} = \mathbf{x}_{\text{pred}} + \mathbf{G}(\mathbf{l} - \mathbf{A}\mathbf{x}_{\text{pred}}), \quad (2.4)$$

$$\mathbf{Q}_{x,\text{adj}} = (\mathbf{I} - \mathbf{G}\mathbf{A})\mathbf{Q}_{x,\text{pred}}, \quad (2.5)$$

with \mathbf{l} as the observation vector and \mathbf{I} denoting the identity matrix.

3. Prediction for the Subsequent Epoch The updated parameters are propagated forward using the system's dynamic model:

$$\mathbf{x}_{\text{pred}, t+1} = \mathbf{T}\mathbf{x}_{\text{adj}}, \quad (2.6)$$

$$\mathbf{Q}_{x,\text{pred}, t+1} = \mathbf{T}\mathbf{Q}_{x,\text{adj}}\mathbf{T}^T + \mathbf{N}, \quad (2.7)$$

where \mathbf{T} is the transition matrix describing the temporal change of the parameters, and \mathbf{N} is the system noise matrix representing the uncertainty of the dynamic model. A larger system noise allows the parameters to vary more freely during the adjustment but also increases the time required for the solution to converge. Conversely, a smaller system noise restricts parameter variation and typically leads to faster convergence. When only a poor initial approximation is available, a larger system noise value is advisable. In addition, suitable initial standard deviations must be specified to initialise the state variance and covariance matrices consistently at the start of the filter.

To ensure stable operation of the filter, unsuitable observations must be removed before processing. As summarised by Glaner (2022), typical exclusion criteria include: low elevation angles, missing satellite orbit or clock information, unavailable bias corrections, poor SNR, detected cycle slips, and general outlier behaviour. Further methodological details on the implementation of the Kalman filter in *raPPPId* are provided by Glaner (2022).

3 Methods

In this chapter, the methodology applied in this study is presented. It explains how the necessary satellite signals are simulated, how the receivers are configured to measure these signals, and how the resulting data are processed.

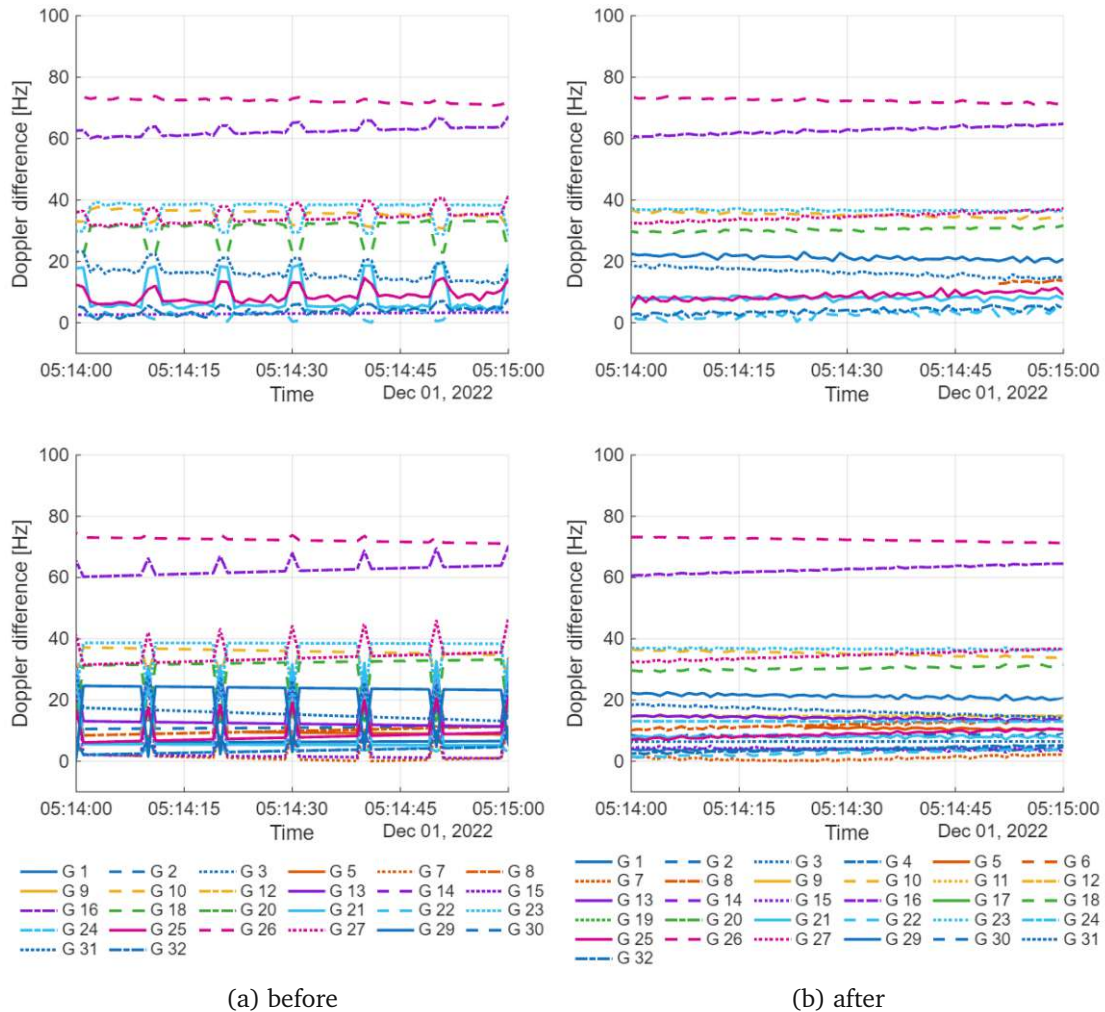


Figure 3.1: Differences in Doppler shift between epochs for each satellite: top row shows the rakon receiver (run 1), bottom row shows the simulated observations; (a) corresponds to measurements before manual interpolation (interpolation performed by the simulator), (b) after the trajectory was interpolated manually.

3.1 Simulation of GNSS Signals

The simulation software *XPLORA* from OHB Austria was used to prepare the simulation files for the GPS upper L-band (L1). The receiver trajectory was derived from Astrocrastr spacecraft

position data provided in 10-second intervals. The simulator internally interpolates these data to 1-second intervals. However, during initial processing, discontinuities at the original 10-second interpolation nodes became apparent in the Doppler Shifts (see Figure 3.1), indicating imperfections in the simulator's interpolation algorithm. To correct this, the trajectory was interpolated externally in MATLAB using the `interp1` function with spline interpolation and then fed into the simulator.

An elevation mask of -20° was applied. Atmospheric delays and multipath effects were disabled, while satellite clock errors were simulated to preserve realistic signal dynamics. The simulated signal was streamed using the IZT S1000 signal generator from OHB Austria.

3.2 Receivers Used in this Study

Two GNSS receivers were used in this work: the u-blox ZED-F9P, listed as "future space-capable receiver" by Gill et al. (2023), and the "RAKON GNSS Development Kit for Nanosatellite Applications", both designed for high-kinematic applications. The F9P firmware was configured by the manufacturer for space applications, with atmospheric corrections disabled, the speed limit removed and satellites below the horizon allowed. According to the manufacturer, the firmware is not intended for high-precision solutions in space. Technical specifications for both receivers are summarised in Table 3.1.

	u-blox	rakon
Price ¹	~130€	-
Weight	1.8 g	6.8 g
Size	17 x 22 x 2.4 mm	31 x 31 x 4.2 mm
Power consumption typ. (max.)	0.26 W (0.47 W)	0.6 W (1.1 W)
Power supply	2.7-3.3 V	3.3 V
Operational temperature	-40°C - 85°C	-40°C - 85°C

¹ in November 2025

Table 3.1: Selected technical specifications of both receivers.

3.3 Measurement Setup

Each GNSS receiver was connected to the OHB Austria simulator via a coaxial cable, while power was supplied through USB from a desktop PC. Part of the setup is shown in Figure 3.2.

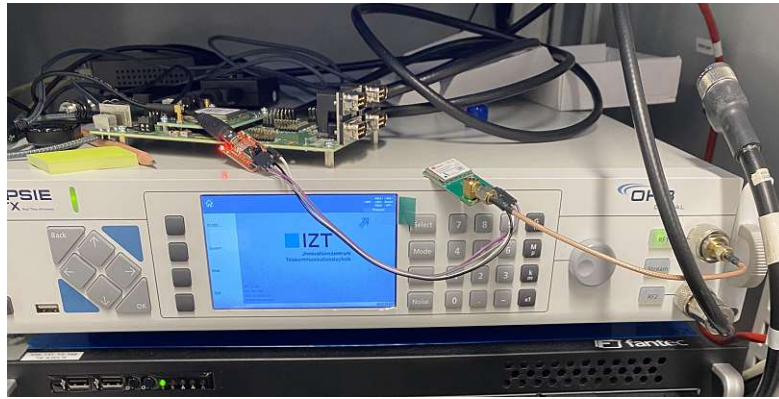


Figure 3.2: Streaming setup.

The satellite tracking was restricted to GPS L1 and the receiver configuration was adjusted to match the space environment and corresponding signal conditions:

- Multipath mitigation disabled (no multipath expected in space)
- Minimum elevation angle set to -20° to guarantee visibility of all simulated satellites
- Tropospheric and ionospheric models disabled
- Motion dynamics parameters (acceleration and jerk) set to maximum

Following an analysis of Doppler observations, the search range was adjusted to ± 45000 Hz, as tests indicated this provided the most reliable tracking performance. The code and carrier tracking loop bandwidths were set to 0.25 Hz (DLL) and 15 Hz (PLL), respectively, based on empirical tuning.

Two power levels were tested (-60 dBm and -100 dBm), which can be set directly on the signal generator, to assess receiver performance under varying signal strengths. The dBm unit expresses power relative to 1 milliwatt, according to

$$P_{\text{dBm}} = 10 \cdot \log_{10} \left(\frac{P_W}{1 \text{ mW}} \right). \quad (3.1)$$

Based on this formula, the corresponding powers in watts are 1 nW for -60 dBm and 0.1 pW for -100 dBm. The signal generator used is not calibrated, and the chosen power levels were selected based on experience to provide realistic received signal strengths for GNSS measurements. Subsequent measurements were conducted at -60 dBm, both under static and kinematic conditions (using the manually interpolated trajectory), and were used to investigate the resulting positioning accuracies.

Each measurement followed an identical procedure:

1. Perform a cold start (u-blox) or hard reset (rakon), clearing all satellite and PVT data. For the u-blox receiver, a full restart of the *u-center* software is required to ensure that all previous clock and satellite data are cleared.
2. Load the correct configuration file.
3. Enable logging.
4. Start simulated signal transmission.
5. After approximately 20 minutes (10 minutes for static measurements), stop logging.
6. Terminate the signal transmission.

3.4 Data Collection

Precise ephemerides (.sp3 files) were used to provide orbit and clock data for the PPP in *raPPPid*. The simulator input consisted of reference coordinates (precise Astrocast CubeSat orbits) in 10-second (from simulator interpolated to 1-second intervals) or 1-second (manual interpolation, see Section 3.1) intervals. Based on these, the simulator generated simulated observation files (RINEX) as well as a computed position solution. The reference and simulated positions were used as ground truth for validation. Furthermore, the simulated observations (RINEX) were also processed using *raPPPid* to obtain comparable PPP-based results. See Figure 3.3 for an overview of the input and output data, as well as the main processing steps.

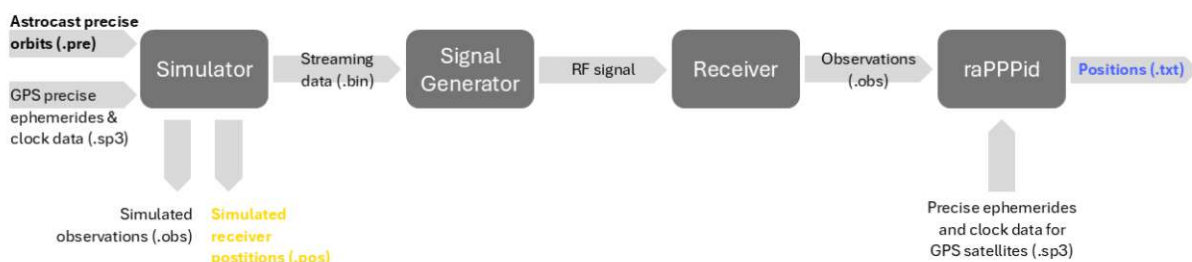


Figure 3.3: In- and outputs of main processing steps.

The simulated GNSS signals were initially transmitted at power levels of -60 dBm and -100 dBm using the original simulation file generated by the simulator, which includes its internal interpolation. Subsequently, additional measurements were performed at -60 dBm using the simulation file in which the trajectory had been manually interpolated to 1-second

intervals, as described in Section 3.1. Finally, static measurements were conducted at -60 dBm, with the receivers remaining stationary in orbit to serve as a reference for assessing whether the receiver can handle altitude and simulated space conditions; here, the lack of velocity ensures that dynamic effects, which are the main challenge, do not interfere.

An overview of all recorded datasets, including the observation durations for each setup, is provided in Table 3.2. Observations obtained with the initial simulation file, in which the trajectory was interpolated by the simulator, were used solely to assess signal tracking performance. For the computation of position solutions, the updated simulation file was used.

The observations from both receivers, originally stored in proprietary file formats, were converted into standard RINEX observation files, ensuring that both C/N_0 and Doppler observations were retained. Only the resulting .obs files were used for subsequent analysis.

	Before ¹		After ²	
	Kinematic -60 dBm	Kinematic -100 dBm	Kinematic -60 dBm	Static -60 dBm
rakon	3 x 20min runs	3 x 20min runs	3 x 20min runs	2 x 10min runs
u-blox	3 x 20min runs	3 x 20min runs	3 x 20min runs	2 x 10min runs

¹ trajectory given in 10s intervals, simulator interpolates to 1s -> used for tracking analysis

² trajectory given in 1s intervals (manually interpolated) -> used for position analysis

Table 3.2: Overview of generated and processed data.

3.5 PPP with *raPPPid*

For precise point positioning, the *raPPPid* software developed at TU Wien was used (Glaner, 2022 and Glaner and Weber, 2023). It is an open-source PPP processing framework that allows full control over model selection and filter configuration. The following processing settings were applied uniformly for all observation files from both receivers:

- Precise orbit and clock information for all GPS satellites obtained from ephemerides files (.sp3)
- All bias corrections disabled
- Ionosphere and troposphere models disabled
- No satellite or receiver phase center offsets or variations
- No corrections for Earth-related effects (solid Earth tides, polar motion, ocean loading)
- No antenna reference point correction

	Initial Std	System Noise	Dynamic Model	
Coordinates:	8000	3000	m/√h	Static Model (Phi ...)
Velocity:	8000	900	m ² /√h	Static Model (Phi ...)
Zenith Wet Delay:	0.1	0.005	m/√h	Static Model (Phi ...)
Receiver Clock GPS:	300000	300000	m/√h	Static Model (Phi ...)
Receiver Clock Glonass:	300000	300000	m/√h	Static Model (Phi ...)
Receiver Clock Galileo:	300000	300000	m/√h	Static Model (Phi ...)
Receiver Clock BeiDou:	300000	300000	m/√h	Static Model (Phi ...)
Receiver Clock QZSS:	300000	300000	m/√h	Static Model (Phi ...)
Receiver DCBs:	3	0	m/√h	Static Model (Phi ...)
Float Ambiguities:	20	0	m/√h	Static Model (Phi ...)
Ionospheric Delay:	1	1	m/√h	Static Model (Phi ...)

<input checked="" type="checkbox"/> Satellite	XXX	ID [3-digit]
	5	Mass [kg]
	0.14	Area [m ²]
	22	Drag coeff [1]
	1.3	Solar coeff [1]

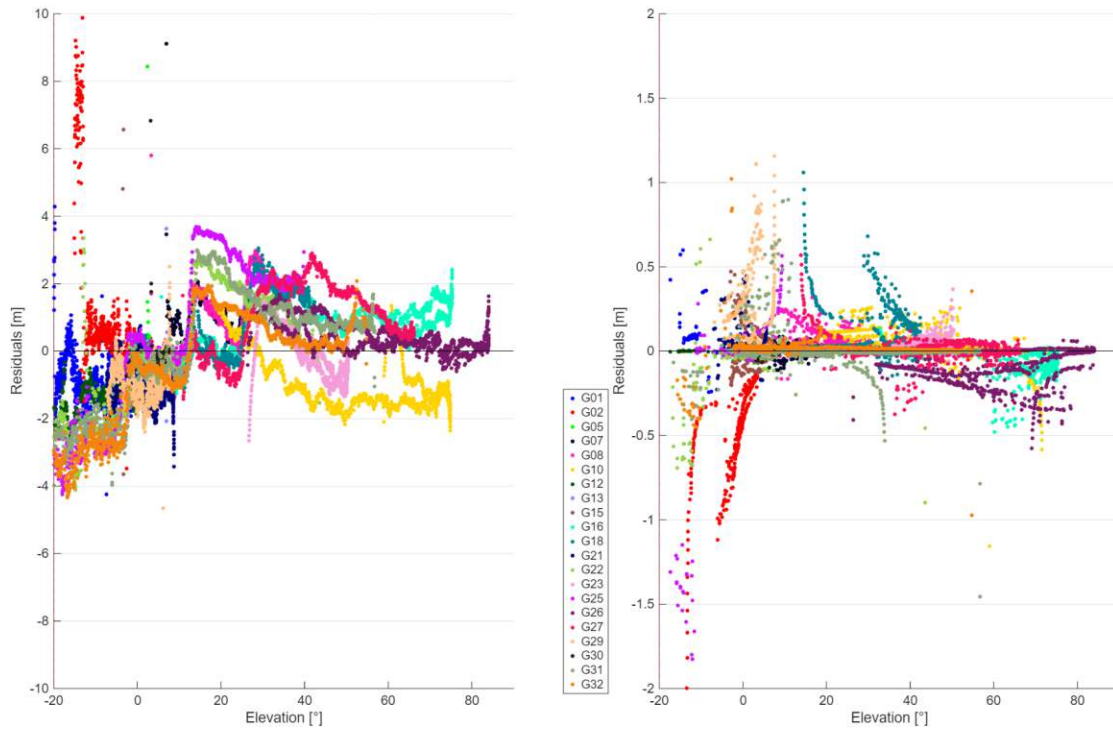
Estimate

Figure 3.4: Overview of default values of the extended Kalman filter in *raPPPId*.

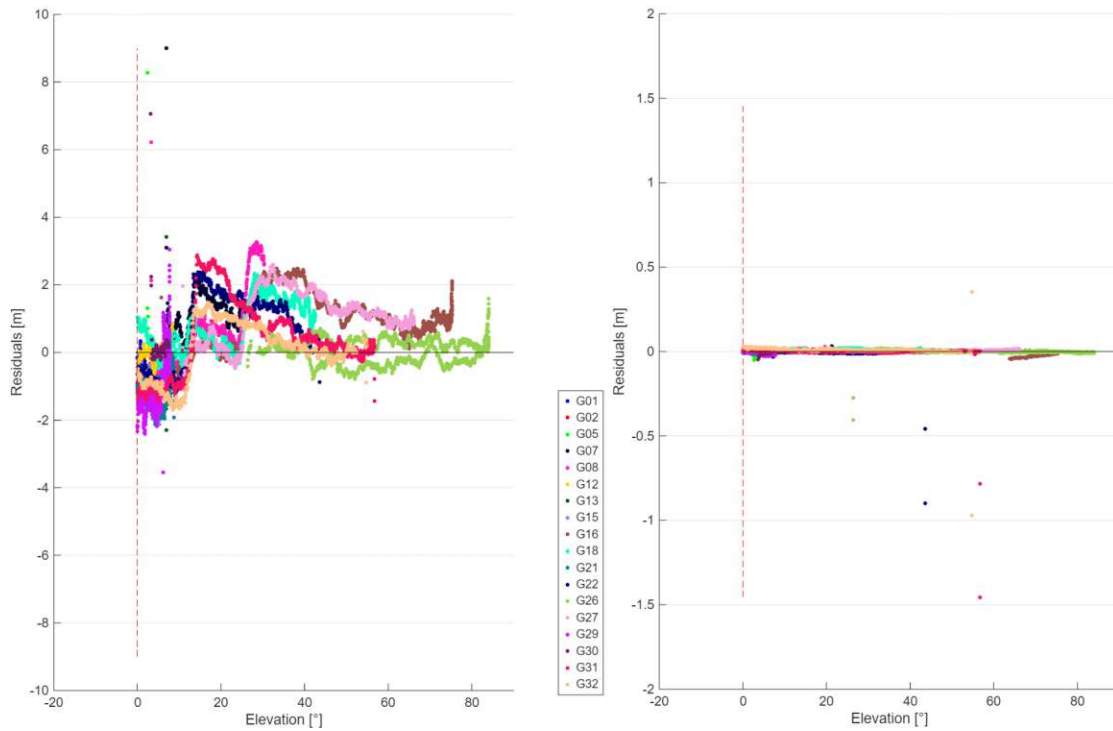
After initial tests, cycle-slip detection was activated (for carrier-phase data) using the time-difference method with a 0.25 m threshold and polynomial degree 3. Ambiguity fixing was not applied. For combined processing of code and phase observations, the extended iterative Kalman filter feature of *raPPPId* (a recent addition to the software) was enabled to estimate receiver position, velocity, and clock parameters at each measurement epoch. Forward filtering was used. To improve performance, satellite-specific parameters such as mass, drag coefficient, cross-sectional area, and solar radiation pressure coefficient were incorporated into the estimation model. In tests, the default values for initial standard deviation, system noise as well as for the satellite-specific parameters (see Figure 3.4) proved to be suitable for all measurements. Although the parameters were varied during preliminary tests, no significant improvements in the results were observed, and therefore the default settings were retained for all subsequent analyses.

The elevation cutoff angle was set to -20° , consistent with the simulation setup. Processing was performed first with code-only data and later with combined code and phase observations. After processing, code and phase residuals were examined to refine the configuration. For the u-blox receiver, the elevation cutoff had to be raised to 0° to achieve stable results (see Tables 4.4 and 4.6). Certain satellites exhibiting irregularities were excluded from processing, for an example of before and after eliminating satellites refer to Figure 3.5. Tables 4.3, 4.4, 4.5 and 4.6 list all excluded satellites.

3 METHODS



(a) Before optimization



(b) After optimization

Figure 3.5: Code (left) and phase (right) residuals of the u-blox receiver (run 1 after manual interpolation) processed in *raPPPid* using (a) basic and (b) optimized configurations.

3.6 Further Processing and Analysis

All subsequent data processing and visualisation were performed in MATLAB. The simulated signal analysis covered the period from 05:00 to 05:20 GPS time. For the positioning analysis, processing was initiated at 05:05 to exclude the receiver initialisation phase and to ensure convergence to a stable solution. Accordingly, the static receiver data span the interval from 05:05 to 05:10, while the kinematic receiver measurements extend from 05:05 to 05:20.

Observation gaps were investigated for each satellite by identifying periods without observations of 1 or more seconds of length to reveal any tracking issues.

The signal-to-noise ratio (SNR) was analyzed with reference to actual GNSS measurements obtained on an Astrocast CubeSat.

Position solutions were evaluated by comparing the simulated positions with the computed positions from *raPPPId*. To eliminate systematic effects presumably introduced by the simulator, which were particularly pronounced in latitude and height, a time-dependent trend was estimated. This trend was obtained by averaging the differences between simulated and computed positions across all receivers for each epoch. The resulting mean trend was subsequently subtracted from the differences, yielding detrended residuals suitable for further analysis.

4 Results

4.1 Tracking Analysis

A detailed tracking analysis was performed for both signal power levels, -60 dBm and -100 dBm. The following subsections present the principal aspects of receiver performance, including satellite visibility, number of valid observations, continuity and speed of tracking, and the number of tracked satellites.

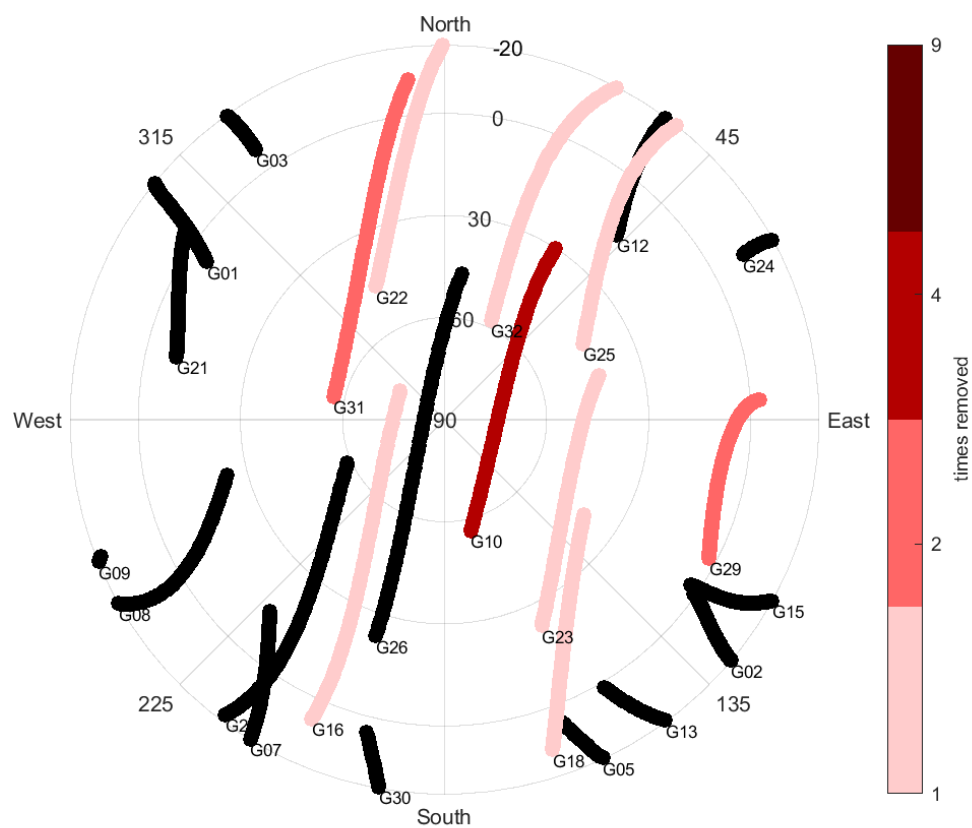


Figure 4.1: Skyplot for the dynamic receiver along the Astrocast trajectory on December 1, 2022 between 5:00 and 5:20 GPS time. Satellites that had to be excluded in any of the observations of both receivers during optimisation of code-only and code-plus-phase processing are highlighted in red. The colour scale indicates how often a satellite was excluded across all twelve processed observation files.

4.1.1 Skyplot

Figure 4.1 illustrates the skyplot of the kinematic receiver along the Astrocast trajectory. Satellites that caused processing issues are highlighted in red. The colour scale represents the frequency with which satellites had to be excluded during the optimisation of the *raPPPId* processing, considering all observation files relevant to the position analysis (both static and kinematic).

Interestingly, most of the problematic satellites are located near the centre of the skyplot, i.e. at higher elevation angles. This is unexpected, as lower elevations are typically more susceptible to signal degradation. The observed pattern may therefore indicate receiver-internal or simulation-specific effects rather than true propagation phenomena.

4.1.2 Number of Observations

Figure 4.2 compares the total number of valid observations recorded by the two receivers with the simulated reference data.

The u-blox receiver recorded approximately 40 % more valid observations than the rakon receiver at a signal power of -60 dBm and around 20 % more at -100 dBm. As expected, a stronger signal power results in a higher number of successful observations.

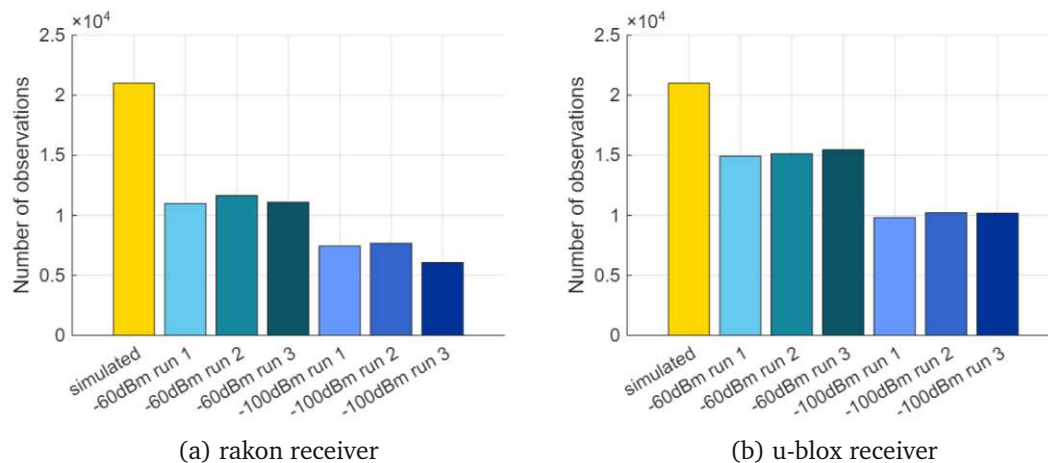


Figure 4.2: Comparison of the number of valid observations per signal-strength level for both receivers. The simulated observations serve as reference.

4.1.3 Observation Gaps

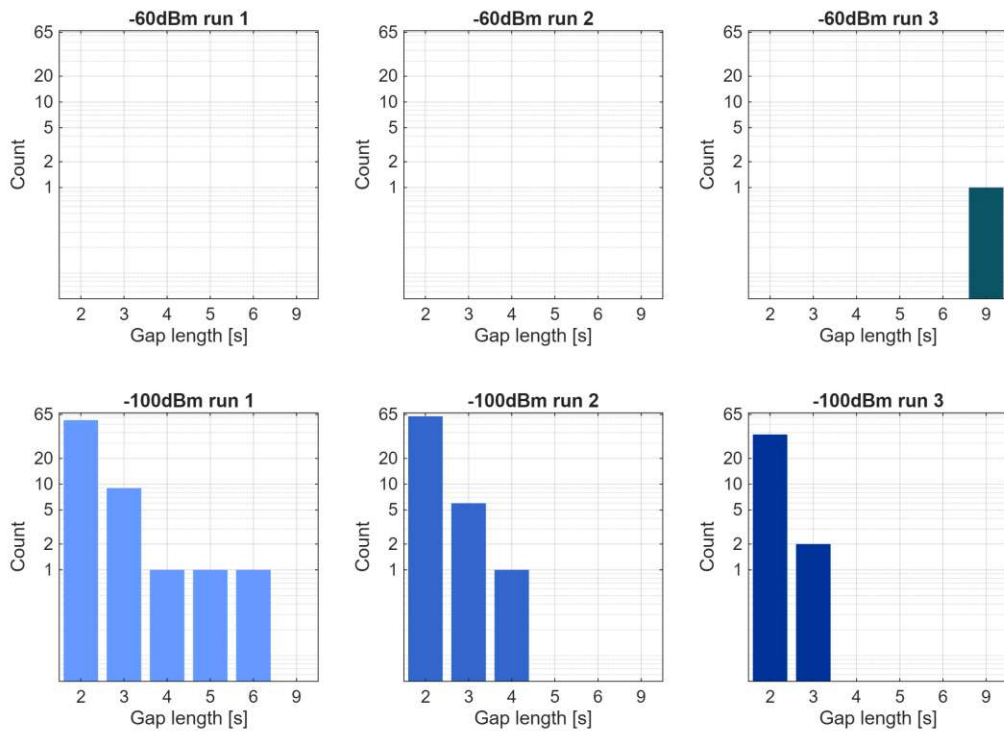
Figure 4.3 shows the distribution of observation gaps longer than 1 s for both receivers, where each bar represents the number of occurrences of a particular gap duration.

4 RESULTS

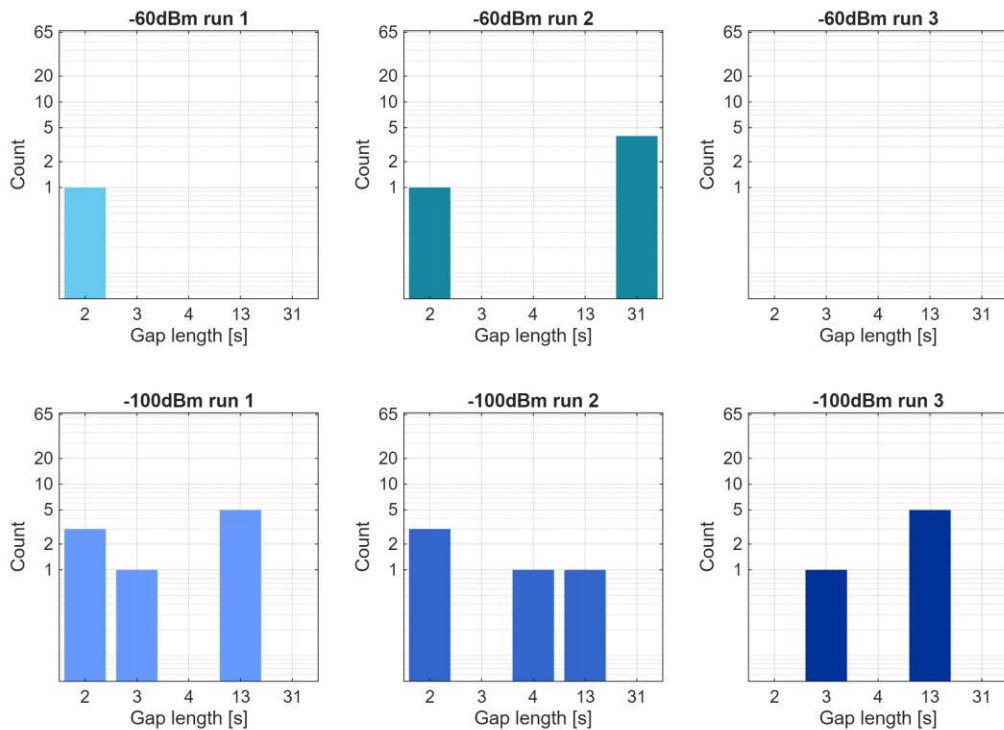
At -60 dBm only a single interruption of 9 s occurred across all three observation files with the rakon receiver, indicating very stable signal tracking. In the observations made with the u-blox receiver, two outages of 2 s and four of 31 s were detected. Run 3 showed no outages.

As signal strength decreases to -100 dBm, both receivers exhibit a higher number of tracking interruptions. For the rakon receiver, a total of 68, 69, and 40 gaps were detected in runs 1, 2, and 3 respectively. Gap durations ranged from 2 s to 6 s, with shorter interruptions being more frequent. For the u-blox receiver, the total number of gaps increased, too (9, 5, and 6 for runs 1–3) and longer interruptions of up to 13 s became more common.

4 RESULTS



(a) rakon receiver



(b) u-blox receiver

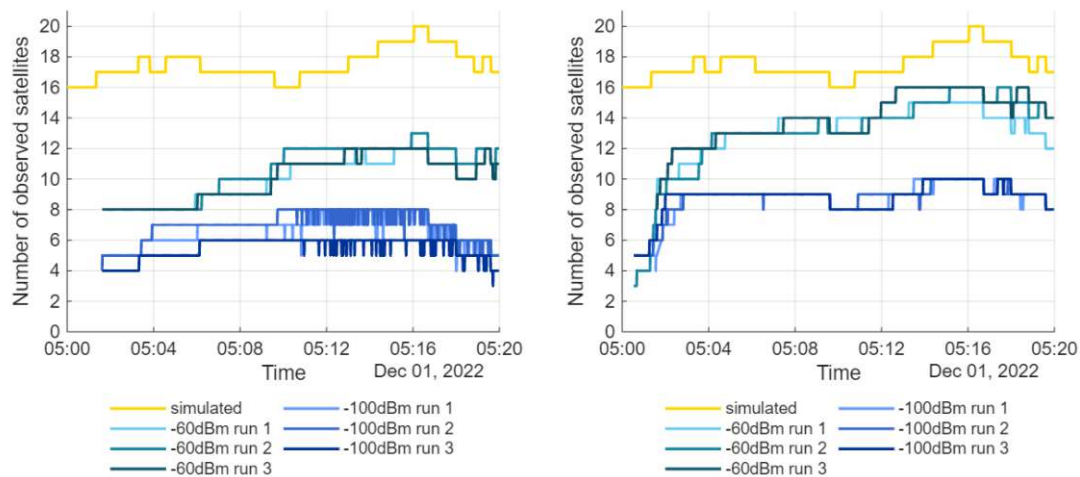
Figure 4.3: Distribution of observation-gap durations for both receivers at different signal-strength levels. Each bar represents the number of gaps of a given duration.

4.1.4 Number of Tracked Satellites

The number of simultaneously tracked satellites during the 20-minute observation period is shown in Figure 4.4. As expected, higher signal strength allows both receivers to track a greater number of satellites. Neither receiver was able to track all simulated satellites.

For the rakon receiver at -60 dBm, at least eight satellites were continuously tracked after the first two minutes. Between ten and thirteen minutes, up to twelve satellites were tracked, and a maximum of sixteen (out of twenty possible) was reached after sixteen minutes during the second run. At -100 dBm, the maximum number dropped to eight satellites for runs 1 and 2 and to six for run 3.

The u-blox receiver generally achieved stable tracking approximately one minute earlier than the rakon receiver for both signal strengths. Overall, it tracked between two and four more satellites on average. At -60 dBm, it consistently tracked at least twelve satellites with a maximum of sixteen, and at -100 dBm it still tracked eight or more — approximately half of all potentially trackable satellites.



(a) rakon receiver

(b) u-blox receiver

Figure 4.4: Number of tracked satellites during the 20-minute observation period for both receivers at different signal-strength levels.

4.1.5 Time Delay to First Tracking

The time delay between satellite rise and first successful tracking provides additional insight into receiver performance. Representative results for both receivers and signal-strength levels are shown in Figure 4.5. Generally, satellites with lower elevation angles exhibit longer delays before tracking is established, indicating a clear correlation between elevation at rise

4 RESULTS

and acquisition latency. Satellites tracked later in the session are also typically those with lower initial elevation, which is partly a consequence of this relationship.

The rakon receiver first acquired a satellite at 05:01:37, while the u-blox receiver did so slightly earlier at 05:01:19. At -100 dBm, the rakon receiver failed to track satellites below roughly 30° elevation, with tracking beginning only above this threshold.

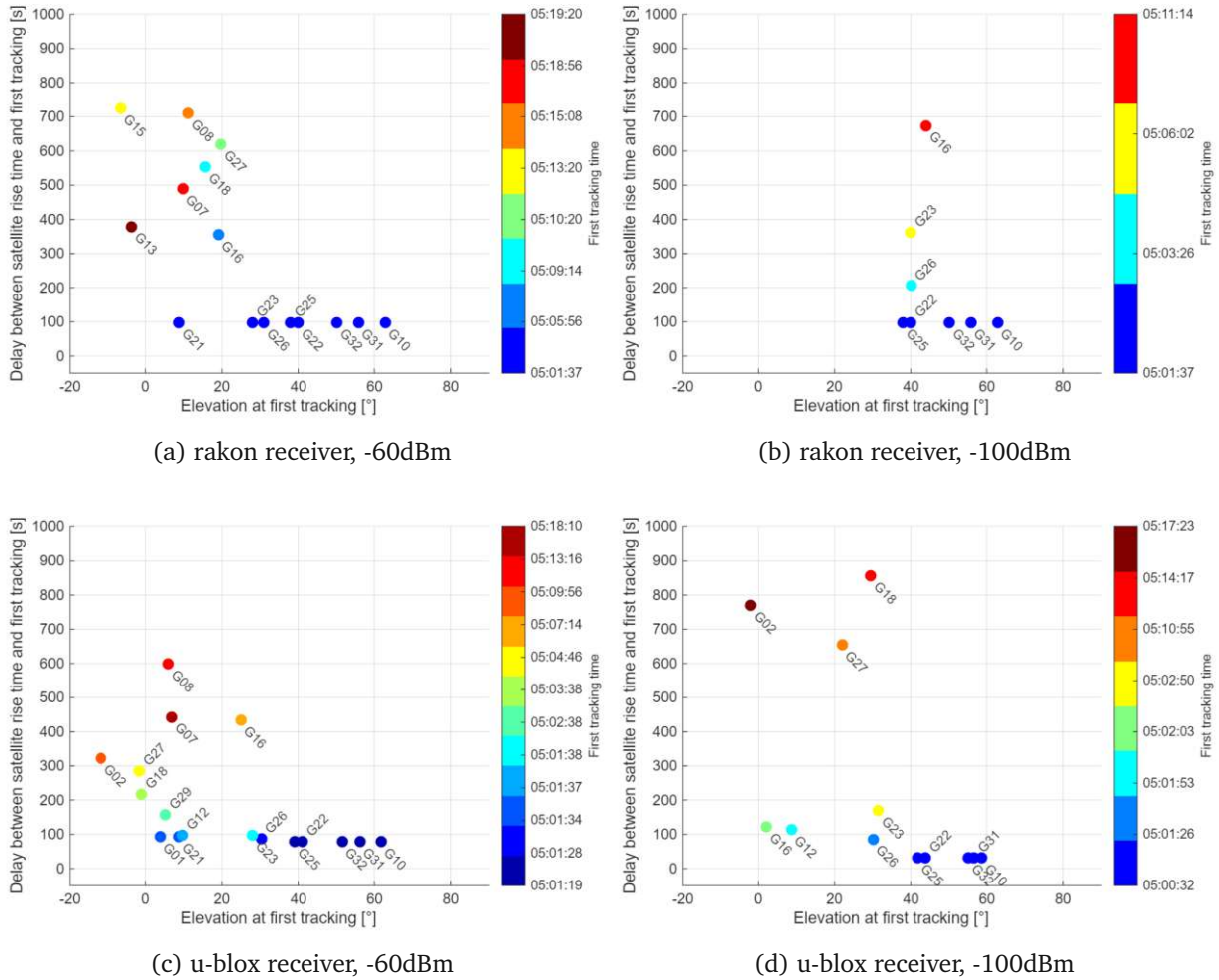


Figure 4.5: Delay between satellite rise at -20° elevation and the first epoch at which the satellite is successfully tracked. The delay is plotted against satellite elevation at rise time. The colour represents the time of first tracking within the observation file: blue indicates satellites tracked early, while red marks those acquired later in the session. Subplots (a)–(d) show representative results for both receivers (rakon and u-blox) at -60 dBm and -100 dBm, respectively.

Median time delays for each satellite are summarised in Table 4.1. At -60 dBm, satellites rising up to 20° exhibited median delays between 97 s and 651.5 s, while satellites above 20° showed a typical median delay of 97 s. At -100 dBm, problematic elevations extended

4 RESULTS

up to 30°, with median delays between 97 s and 835 s; above 30°, delays ranged from 94.5 s to 188 s. No significant correlation was found between delay and azimuth at rise time.

Satellite ID	Median delay ¹ [s]	Median delay ¹ [min:s]	Median elevation ² [°]	Median azimuth ² [°]
15	651.5	10:51	-8.11	122.45
2	487.0	08:07	-7.89	127.65
13	379.0	06:19	-3.55	148.54
1	127.0	02:07	3.10	304.79
29	209.0	03:29	5.89	110.78
8	615.5	10:15	6.86	241.71
7	469.0	07:49	8.52	219.27
21	97.0	01:37	8.77	284.80
12	97.0	01:37	9.72	40.54
27	507.0	08:27	12.27	215.17
18	549.5	09:09	15.46	152.08
16	359.0	05:59	19.28	204.39
23	97.0	01:37	28.00	151.29
26	97.0	01:37	31.02	197.76
25	97.0	01:37	38.03	54.29
22	97.0	01:37	40.06	337.93
32	97.0	01:37	50.16	23.00
31	97.0	01:37	55.88	295.59
10	97.0	01:37	62.85	159.51

¹time delay from satellite crossing -20° elevation

²of satellite at first tracking

(a) -60dBm

Satellite ID	Median delay ¹ [s]	Median delay ¹ [min:s]	Median elevation ² [°]	Median azimuth ² [°]
2	769.0	12:49	-1.96	125.68
16	123.0	02:03	2.17	203.62
12	97.0	01:37	9.72	40.54
27	740.0	12:20	27.80	218.58
18	835.0	13:55	28.59	142.81
23	188.0	03:08	32.37	147.54
26	172.5	02:52	37.29	198.11
25	97.0	01:37	38.03	54.29
22	94.5	01:34	40.21	337.81
32	97.0	01:37	50.16	23.00
31	94.5	01:34	55.93	295.24
10	94.5	01:34	62.69	159.73

¹time delay from satellite crossing -20° elevation

²of satellite at first tracking

(b) -100dBm

Table 4.1: Calculated median time delays between satellite rise time and first tracking at -60 dBm (a) and -100 dBm (b) across all observations of both receivers. Median elevation and azimuth are calculated for the position of first tracking. The tables are sorted by elevation.

4.2 Signal Analysis

In this section, the influence of signal strength and the corresponding Carrier-to-Noise Density Ratio (C/N_0) are examined in detail. Both parameters are fundamental indicators of receiver performance and directly affect tracking stability and positioning precision.

4.2.1 Distribution of C/N_0

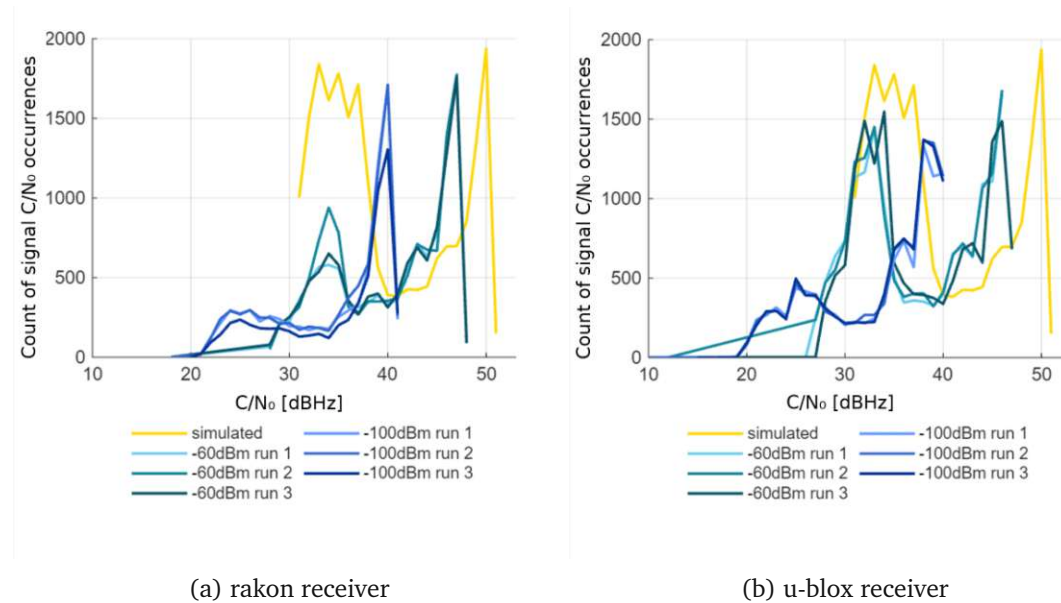


Figure 4.6: Distribution of C/N_0 for both receivers. For each C/N_0 , the number of occurrences is counted.

The simulated reference observations exhibit two prominent peaks in C/N_0 occurrence: one between 32 dBHz and 38 dBHz, and a second at approximately 50 dBHz. For all observation runs and both receivers, one clear peak is visible; however, it is shifted to lower values by about 3 dBHz at -60 dBm and by roughly 10 dBHz at -100 dBm.

For the *rakon* receiver, the secondary peak at -60 dBm is less pronounced, occurring around 35 dBHz, and is nearly smoothed out at -100 dBm near 25 dBHz. In contrast, the *u-blox* receiver shows a more distinct secondary maximum: at -60 dBm the two peaks are of similar height, centred around 32 dBHz, whereas at -100 dBm the secondary peak diminishes substantially and shifts to approximately 25 dBHz. These distributions, summarised in Figure 4.6, confirm the expected reduction in received signal power as the input level decreases.

4.2.2 Carrier-to-Noise Density Ratio

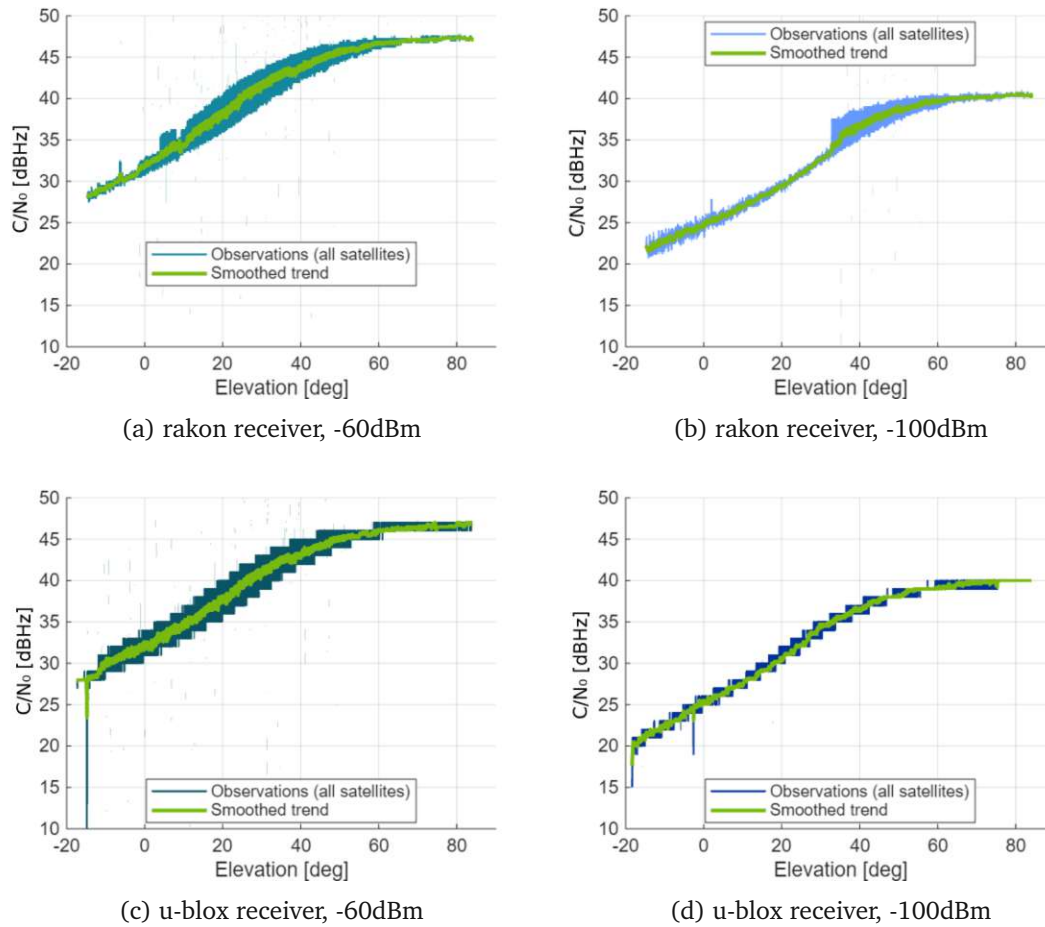


Figure 4.7: Comparison of C/N_0 versus satellite elevation for *rakon* (top row) and *u-blox* (bottom row) receivers at -60 dBm (left) and -100 dBm (right).

The C/N_0 behaviour shown in Figure 4.7 follows the expected relationship between signal strength and satellite elevation. For the *rakon* receiver, C/N_0 values range from approximately 26 to 47 dBHz at -60 dBm and from 22 to 40 dBHz at -100 dBm. The *u-blox* receiver exhibits comparable C/N_0 levels, between 25 and 46 dBHz at -60 dBm and between 20 and 40 dBHz at -100 dBm. In all configurations, C/N_0 increases with satellite elevation: lower elevations are associated with reduced values, whereas C/N_0 saturates above approximately 55 – 60° elevation. As expected, lower input signal power results in uniformly reduced C/N_0 across all elevations.

		rakon			u-blox			
		Run 1	Run 2	Run 3	Run 1	Run 2	Run 3	Median
		-60dBm						
σ (w/o outliers)	C1C [m]	0.956	1.027	0.977	0.710	3868.778	1.137	1.002
	L1C [m]	0.851	0.886	0.859	0.528	4510.504	1.007	0.873
	D1C [Hz]	4.154	4.739	4.372	5.078	5.906	5.099	4.909
		-100dBm						
σ (w/o outliers)	C1C [m]	1.377	1.275	1.332	1.622	1.244	1.820	1.355
	L1C [m]	0.538	0.472	0.521	0.829	0.550	81.219	0.544
	D1C [Hz]	3.163	3.006	3.049	8.271	5.012	9.494	4.088

Table 4.2: Noise characteristics of time-differenced GPS L1 observations (C1C, L1C, D1C) for both receivers and signal levels.

To assess the quality of the raw observations, time-differenced GPS L1 measurements (C1C, L1C, D1C) were analysed (Table 4.2). The standard deviation of these differences provides a measure of noise level and temporal stability. Across all measurement runs and both receiver types, the median standard deviations (excluding outliers) were approximately 1.00 m for the code pseudorange (C1C), 0.87 m for the carrier phase (L1C), and 4.91 m (5 Hz) for the Doppler (D1C) observations at -60 dBm. For the lower signal strength of -100 dBm, the respective median values increased slightly to 1.36 m (C1C), 0.54 m (L1C), and 4.09 Hz (D1C).

4.3 Position Solution with Code Observations

4.3.1 Static Receiver

For the static receiver, the code-only position solution (see Table 4.3) shows a standard deviation of approximately 1 m for the *u-blox* receiver when using basic processing. After optimisation, achieved by removing selected satellites, the standard deviation improves to about 0.5 m. For the *rakon* receiver, the basic processing already results in a standard deviation of approximately 0.19 m, and no further optimisation was achieved by removing selected satellites.

Regarding the residuals over time, defined as the difference between simulated and calculated position, the values generally scatter around 0 m (see green trend line in Figure 4.8). No temporal drift is visible. For the *u-blox* receiver, a slightly positive dispersion is observed in latitude, while the *rakon* receiver shows a small negative offset. In latitude, most values lie between -0.5 m and 0.5 m, with a single outlier near 2 m. In longitude, the *u-blox* data exhibit slightly larger negative residuals than the *rakon* data, although most values remain within ± 0.5 m and no extreme outliers occur. In height, most *u-blox* residuals fall between -2 m and 2 m, while all *rakon* residuals are within ± 1 m.

4 RESULTS

Processing		Basic ¹	Optimised ²		
Receiver	Run	σ code [m]	σ code [m]	Removed satellites	Cutoff elevation [°]
u-blox	1	0.935	0.459	G18, G27	-20
	2	1.013	0.531	G18, G27	-20
rakon	1	0.196	no optimisation necessary		
	2	0.186			

¹ cutoff elevation -20°

² removing satellites, adapting cutoff elevation

Table 4.3: Residuals and optimisation parameters of the static position solution.

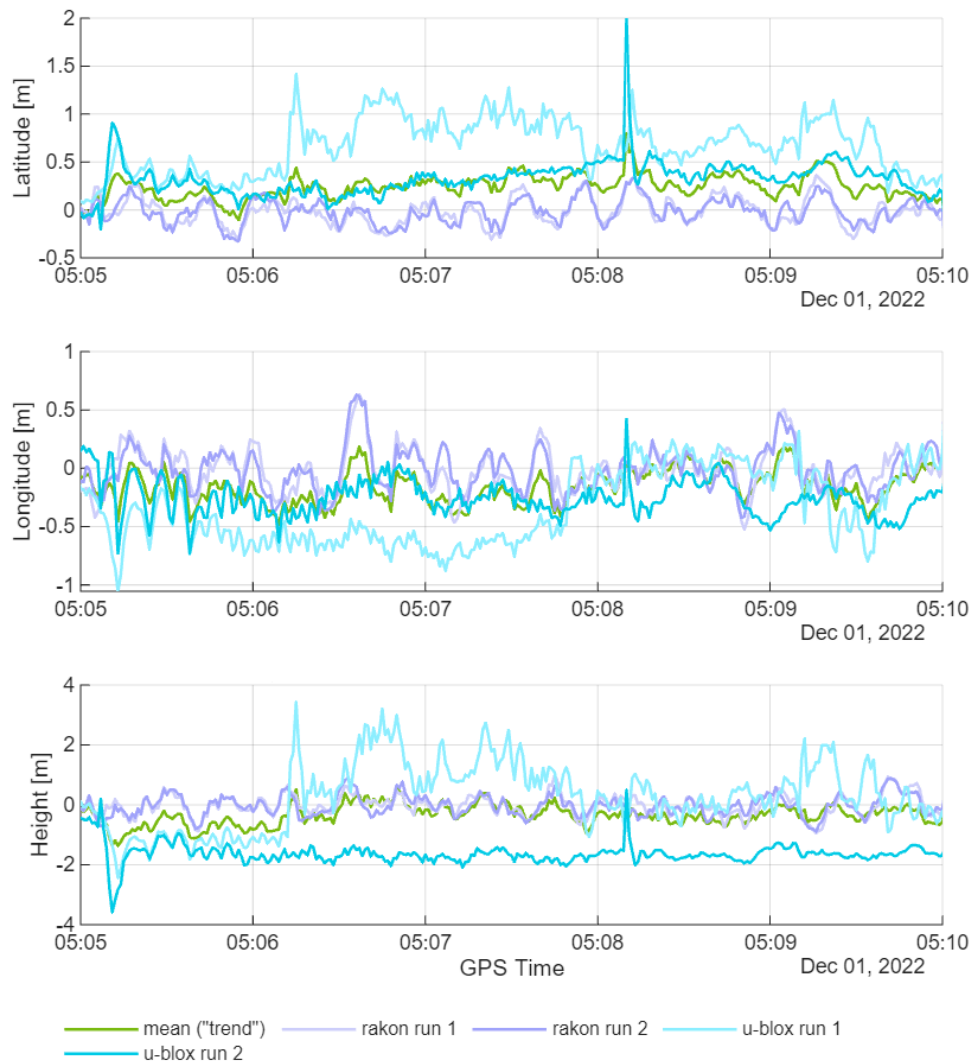


Figure 4.8: Differences between simulated position and position calculated from observations in latitude, longitude, and height.

4.3.2 Kinematic Receiver

For the kinematic receiver, the same analysis was performed using code-only observations (see Table 4.4). The *u-blox* receiver shows a standard deviation of approximately 1 m with basic processing and about 0.7–0.8 m after optimisation. During the optimisation, several satellites were excluded and the elevation cutoff was increased to 0°. For the *rakon* receiver, no optimisation was necessary; the standard deviation is about 0.37 m.

Processing	Run	Basic ¹ σ code [m]	Optimised ² σ code [m]	Removed satellites	Cutoff elevation [°]
<i>u-blox</i>	1	1.034	0.837	G31	0
	2	0.981	0.727	G10, G31	0
	3	0.986	0.717	G10, G31	0
<i>rakon</i>	1	0.378	no optimisation necessary		
	2	0.377			
	3	0.369			

¹ cutoff elevation -20°

² removing satellites, adapting cutoff elevation

Table 4.4: Residuals and optimisation parameters of the kinematic code measurements.

Considering the differences between the reference and calculated positions (Figure 4.9), the latitude residuals for the *rakon* receiver range from approximately -4 to 2 m, while the *u-blox* receiver shows values from about -3 to 3.5 m (up to 5 m including one outlier). A time-dependent trend is visible, with the residuals drifting from negative towards positive values.

In longitude, the residuals fluctuate around 0 m. For the *rakon* receiver, they range roughly within ± 1 m without time-dependent variation. For the *u-blox* receiver, the values start around -1 m and vary between 0 and approximately 0.5 m after $05:08:30$, excluding outliers.

In height, the residuals do not oscillate around zero. For the *rakon* receiver, most values are distributed around -1.25 m (typically between -2.5 and 0 m). For the *u-blox* receiver, three distinct time intervals can be identified, showing slight temporal drifts: from $05:00$ to approximately $05:08$ residuals scatter around -6 m; between $05:08$ and $05:18$ around -5 m; and from $05:18$ to $05:20$ again around -6 m. The variation within these intervals is less pronounced than for the *rakon* receiver.

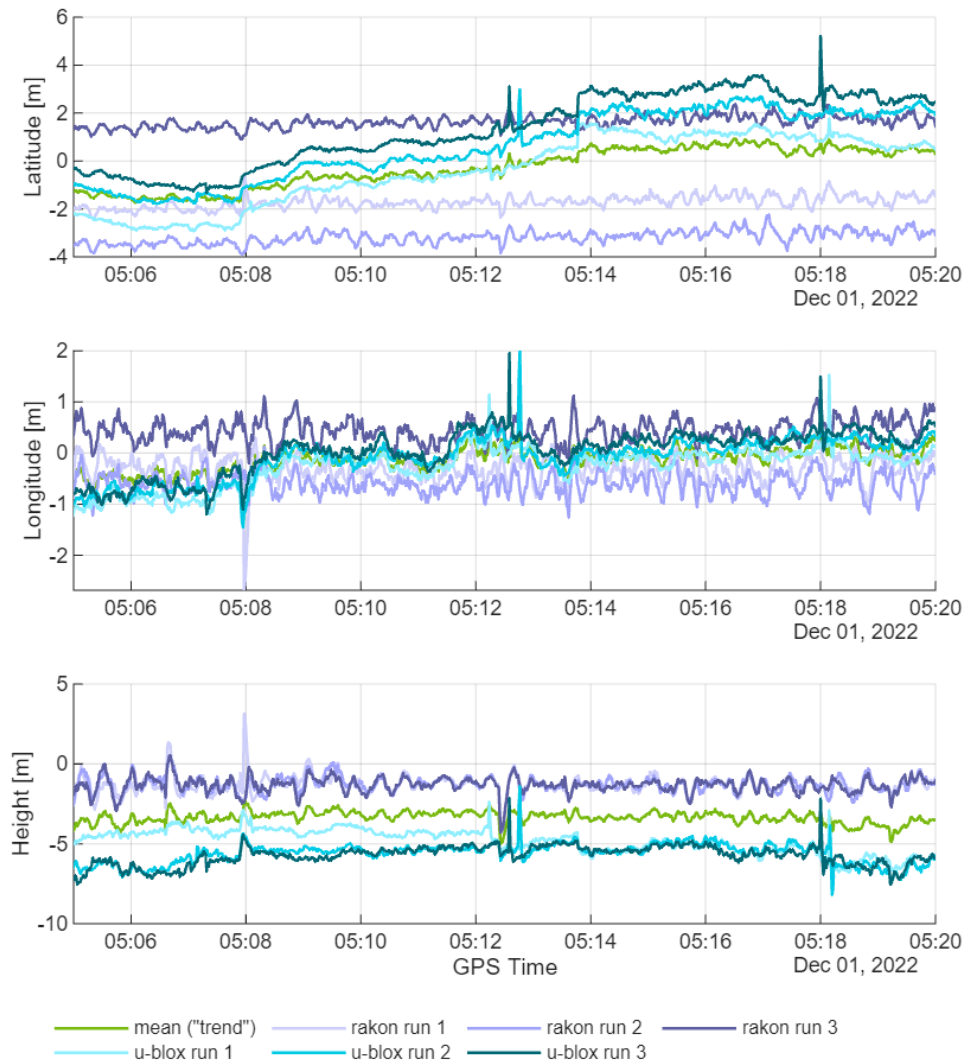


Figure 4.9: Differences between simulated position and position calculated from observations in latitude, longitude, and height.

Due to the temporal trends (drifts), the mean value (trend) was subtracted to remove them (see Figure 4.10). After detrending, the latitude residuals range between -3 and 3 m and scatter around zero. Longitude residuals also oscillate around zero, with most values within ± 1 m. In height, the *rakon* data scatter around 2.5 m and the *u-blox* data around -2.5 m.

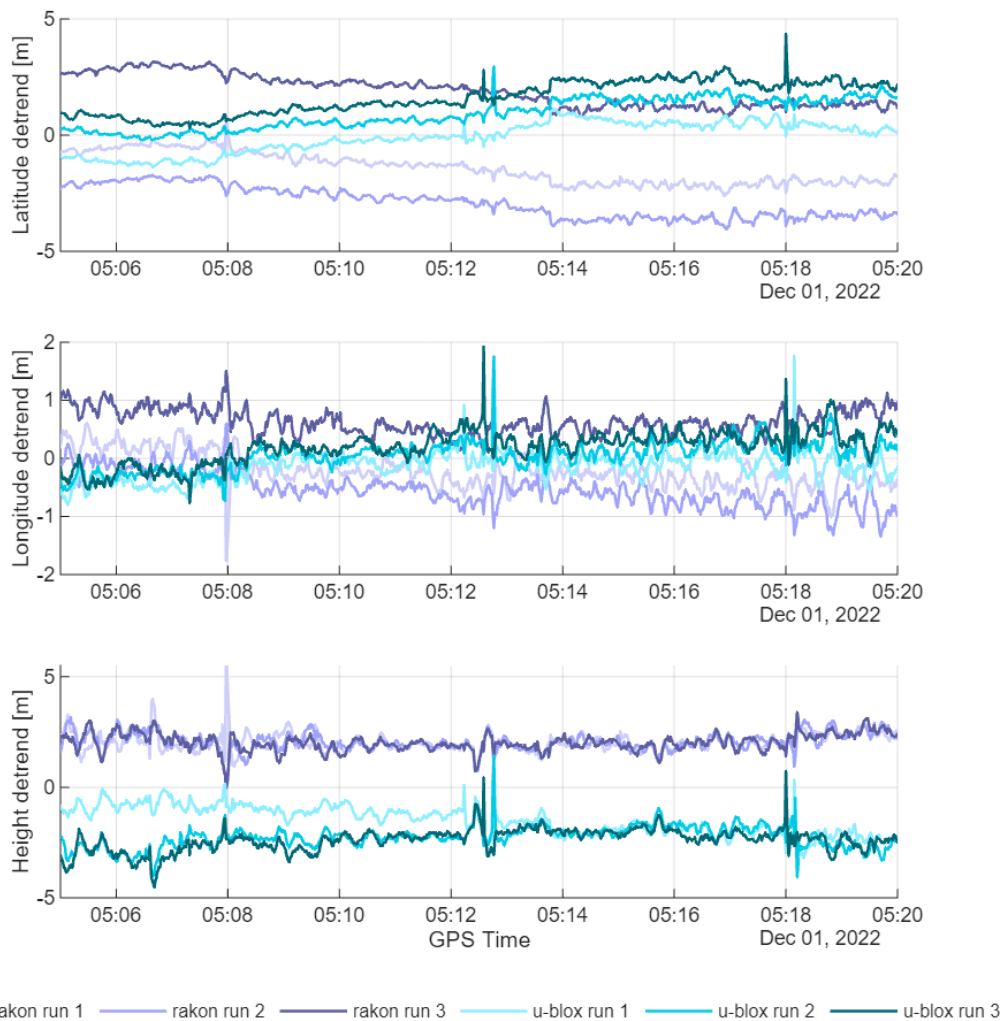


Figure 4.10: Differences in position (latitude, longitude, height) between simulated position and calculated position with trend removed.

4.4 Position Solution with Code and Phase Observations

4.4.1 Static Receiver

For the static receiver, combined code and carrier phase observations were processed. The standard deviations are summarised in Table 4.5. For the *u-blox* receiver, the code-only solution shows values of approximately 1.1 and 2.1 m, whereas the combined code and phase solution improves to 0.005 and 0.37 m (basic processing). After optimisation, by removing selected satellites, the standard deviations are about 0.7 m for the code and 0.005 m for the phase solution. For the *rakon* receiver, the basic solution yields about 0.27 m for the code and 0.002 m for the phase. After optimisation, the values improve to approximately 0.19 m (code) and 0.002 m (phase).

4 RESULTS

Processing		Basic ¹		Optimised ²			
Receiver	Run	σ code [m]	σ phase [m]	σ code [m]	σ phase [m]	Removed satellites	Cutoff elevation [°]
u-blox	1	1.119	0.005	0.653	0.005	G18, G27	-20
	2	2.126	0.373	0.744	0.005	G18, G24, G27	-20
rakon	1	0.274	0.002	0.212	0.002	G21, G29	-20
	2	0.269	0.002	0.175	0.002	G12, G21, G29	-20

¹ cutoff elevation -20°, no cycle slip detection, no phase wind up correction

² cycle slip detection, phase wind up correction

Table 4.5: Residuals and optimisation parameters of static measurements using code and phase.

The differences between reference and calculated positions (Figure 4.11) show that, in all three coordinates, both *u-blox* runs deviate more from each other than the two *rakon* runs. In latitude, the residuals do not scatter around zero. A slight upward trend (drift from 0.01 to 0.05 m) is visible for the *rakon* receiver, and a downward trend (from 0.03–0.055 m to 0.015–0.03 m) for the *u-blox*. In longitude, all results show a slight upward trend: for the *rakon* receiver starting around 0 and increasing up to 0.015 m, and for the *u-blox* receiver approaching zero from initial values of approximately –0.2 or 0.1 m. In height, values lie between –0.05 and –0.2 m, with both receivers showing a small downward drift over time.

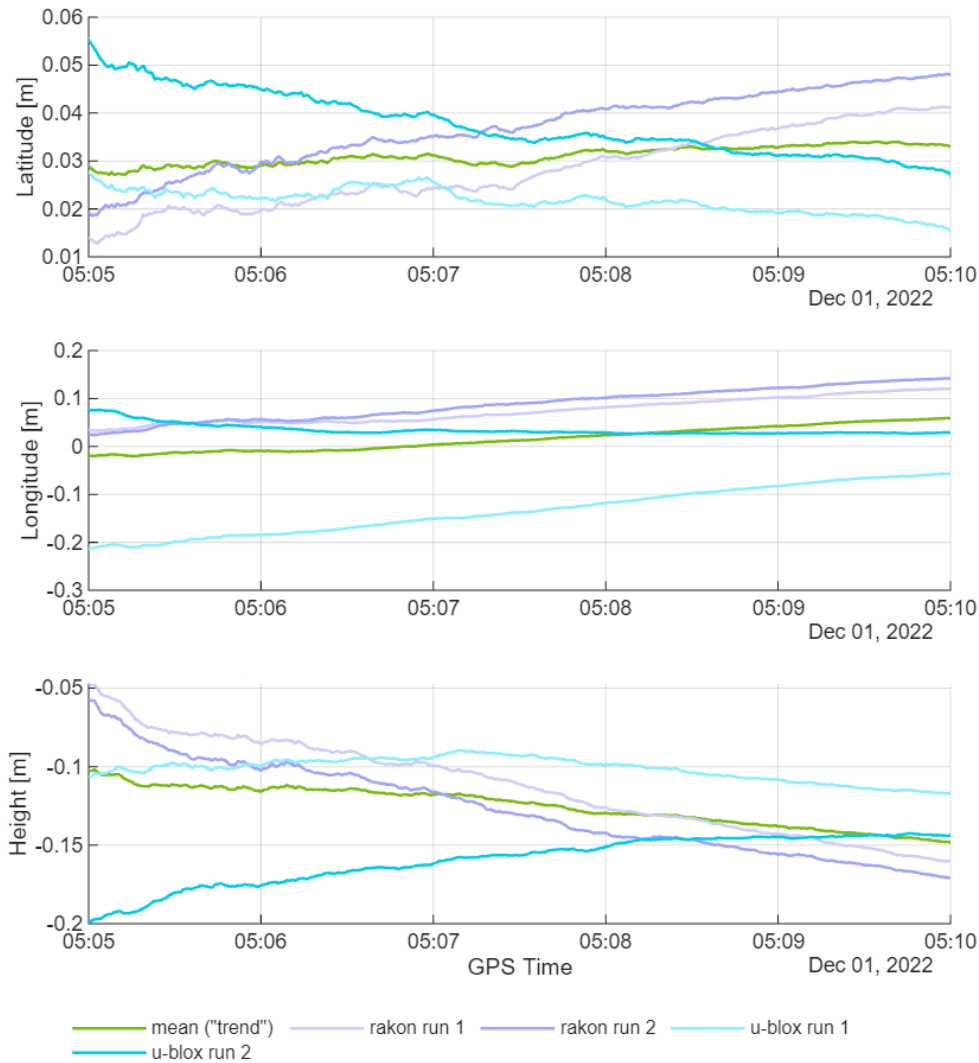


Figure 4.11: Differences between simulated position and position calculated from observations in latitude, longitude, and height.

To remove these drifts, the mean value was subtracted (see Figure 4.12). After detrending, the overall scatter improves in all three coordinates. Opposite trends in latitude and height are naturally not eliminated, but the residuals now generally cluster around 0 m with smaller magnitudes.

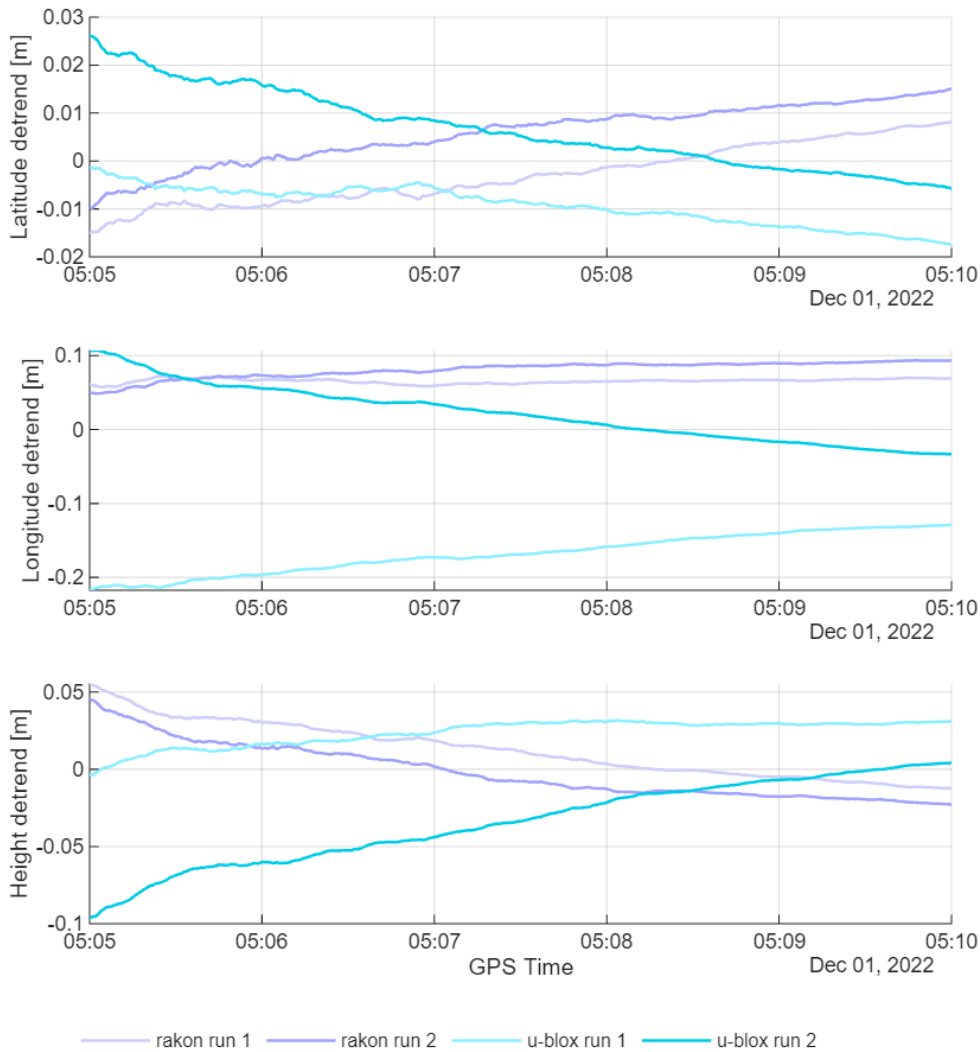


Figure 4.12: Differences in position (latitude, longitude, height) between simulated position and calculated position with trend removed.

4.4.2 Kinematic Receiver

For the kinematic receiver using combined code and phase observations, the standard deviations are listed in Table 4.6. For the *u-blox* receiver, basic processing results in residuals of approximately 1.5 m for the code and 0.08–0.23 m for the phase. After optimisation, with removed satellites and an elevation cutoff of 0° instead of -20° , the standard deviations are about 1.1 m (code) and 0.02–0.04 m (phase). For the *rakon* receiver, the basic solution gives residuals of around 1.0 m for the code and 0.04–0.05 m for the phase. After optimisation (only satellite removal), runs 1 and 2 show values between 0.9 and 1.0 m for the code and 0.03–0.05 m for the phase. For run 3, the code standard deviation increases slightly to

4 RESULTS

1.177 m.

Processing		Basic ¹		Optimised ²			
Receiver	Run	σ code [m]	σ phase [m]	σ code [m]	σ phase [m]	Removed satellites	Cutoff elevation [°]
u-blox	1	1.431	0.146	1.072	0.024	G10, G23, G25	0
	2	1.719	0.230	1.183	0.044	G1, G18, G22, G32	0
	3	1.459	0.079	1.099	0.031	G10	0
rakon	1	1.055	0.052	0.983	0.052	G10	-20
	2	1.041	0.038	0.898	0.035	G10, G29	-20
	3	1.088	0.047	1.177	0.045	G10, G16, G29	-20

¹ cutoff elevation -20°, no cycle slip detection, no phase wind up correction

² cycle slip detection, phase wind up correction

Table 4.6: Residuals and optimisation parameters of kinematic measurements using code and phase.

The differences between simulated and calculated positions (Figure 4.13) show a strong downward trend (drift away from the reference solution) in latitude for all measurement runs and both receivers, from approximately 0 to -1.5 m. In longitude, a periodic variation is visible, resembling a sine wave between -0.6 and 0.2 m for both receivers. The *rakon* receiver oscillates between -0.2 and 0.2 m, while the *u-blox* varies between -0.6 and 0 m. The overall mean for both receivers is around -0.2 m. In height, a strong negative offset is observed, with differences between approximately -3 and -6 m, along with a trend towards zero over time. For the *rakon* receiver, values first lie near -4 m, decrease to about -4.5 m around 05:09, and then rise again. For the *u-blox* receiver, the residuals increase steadily from -6 m to -3 m.

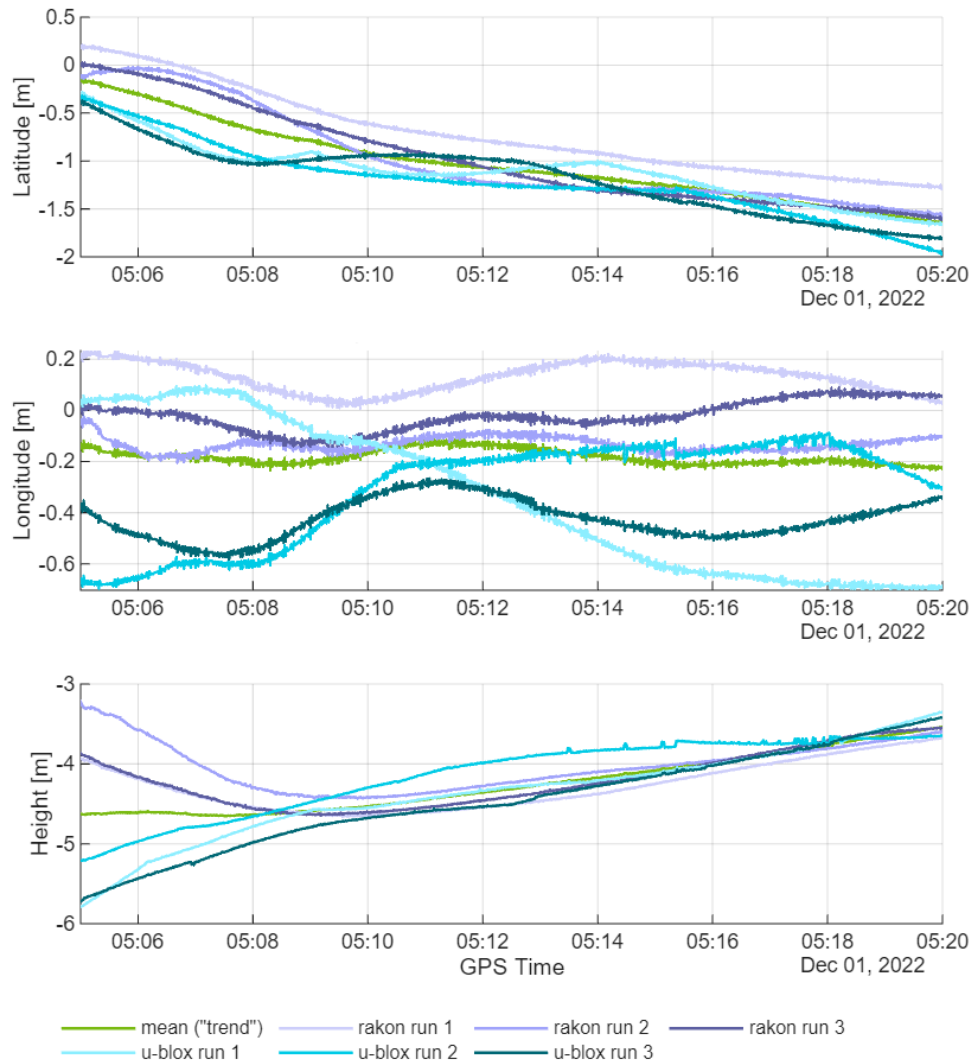


Figure 4.13: Differences between simulated position and position calculated from observations in latitude, longitude, and height.

After subtracting the mean values to remove temporal trends (see Figure 4.14), all three coordinates scatter around zero. In latitude and longitude, the magnitude of scatter varies over time in a sinusoidal manner between approximately ± 0.5 m. In height, the residuals converge towards zero and then fluctuate between approximately -0.15 m and 0.15 m.

4 RESULTS

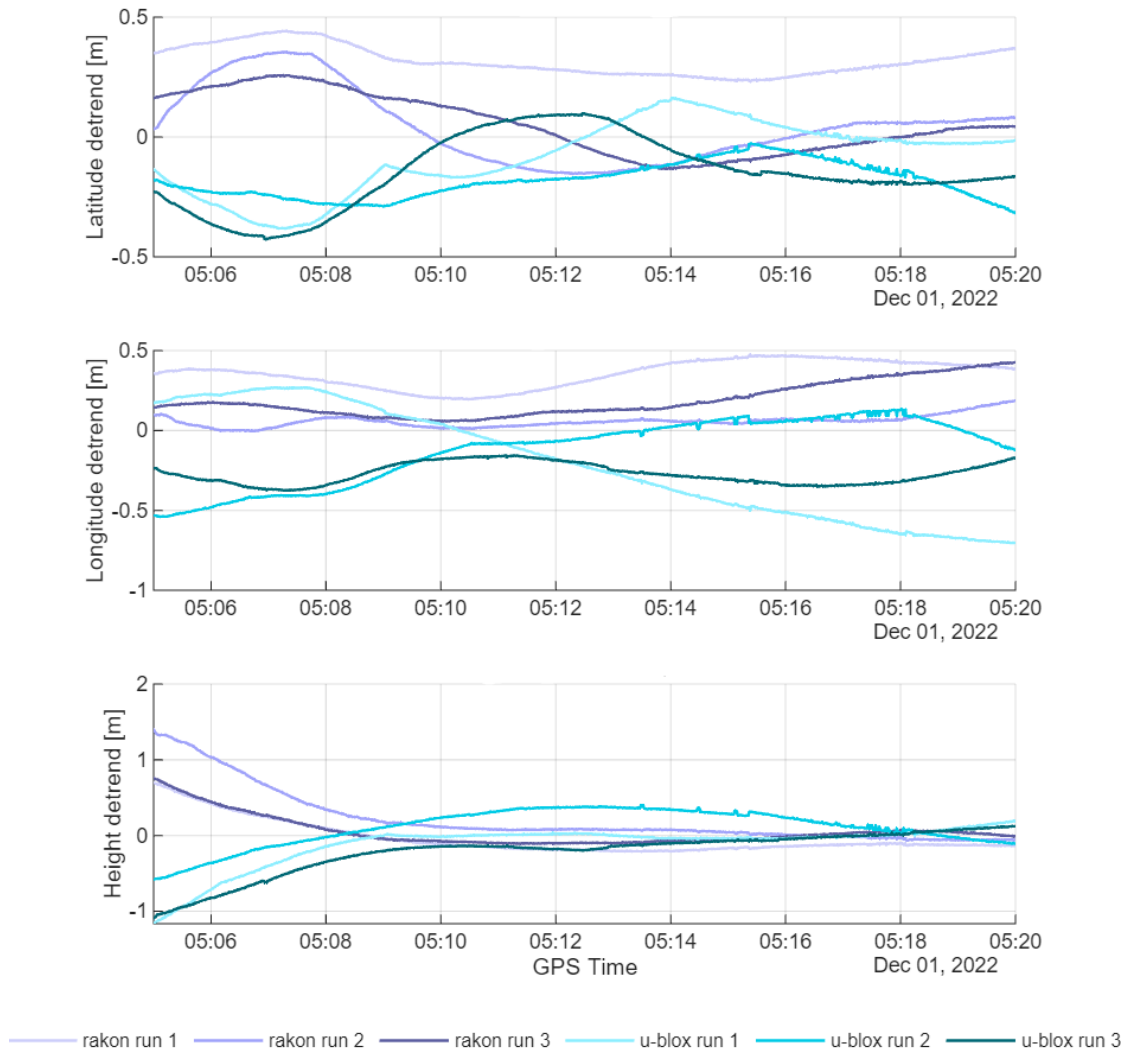


Figure 4.14: Differences in position (latitude, longitude, height) between simulated position and calculated position with trend removed.

5 Discussion

5.1 Signal and Tracking

The simulated signal strength had a direct impact on the receiver's C/N_0 and tracking performance. At -100 dBm, the C/N_0 was considerably lower, resulting in reduced signal quality, fewer visible satellites, longer and more frequent data gaps, and an overall decrease in the number of observations. These effects are in line with expectations (see Figures 4.2, 4.3, 4.4, 4.6 and 4.7). The lower signal quality at -100 dBm explains the increased number of tracking interruptions and the extended acquisition times discussed in Section 4.1.

Comparing C/N_0 values from the simulation (Figure 4.7) with real measurements (Figure 5.1) shows that real values observed on board of an Astrocast CubeSat range between 27.5 and 38 dBHz, whereas simulated values span a broader range from 20 to 45 dBHz, indicating that the simulation captures typical signal variability.

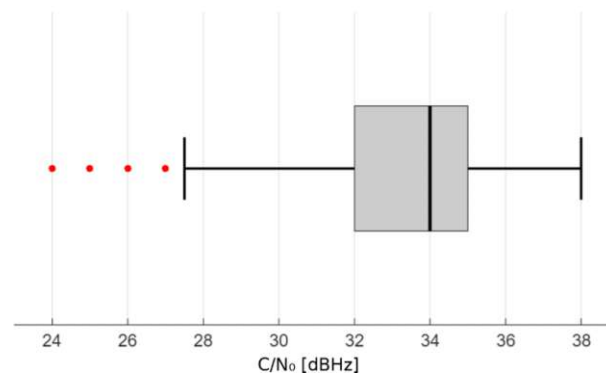


Figure 5.1: Boxplot of real observed C/N_0 values on board an Astrocast CubeSat nanosatellite. Outliers are marked in red.

The time delay between signal rise and the moment of first tracking is primarily influenced by satellite elevation rather than signal strength (see Figures 4.5 and Table 4.1). Nevertheless, C/N_0 and elevation are correlated (Figure 4.7): lower elevation corresponds to lower C/N_0 , which indirectly affects tracking performance.

Analysis of measurement noise reveals that C1C noise increases at -100 dBm (Table 4.2), while L1C and D1C noise appear reduced at the same signal level. These results are consistent with typical GPS L1 noise characteristics under controlled reception conditions and demonstrate good internal consistency of the simulated RINEX data. Occasional outliers, particularly in the *u-blox* data, can be attributed to temporary loss of lock, causing discontinuities in the raw measurements. Such events are expected under weak-signal conditions, when the receiver tracking loops momentarily lose synchronisation or reset their internal filters.

5.2 Position Solution

As expected, position solutions computed using code-only observations performed worse (metric-level accuracy) compared to solutions using both code and carrier-phase observations (centimetre- to decimetre-level accuracy in the horizontal plane, metre-level in height), as discussed in Sections 4.3 and 4.4.

Position solutions for the static receiver achieved centimetre- to decimetre-level accuracy, whereas the kinematic receiver yielded decimetre- to metre-level results. The discrepancy between static and kinematic solutions indicates potential limitations in the simulator's handling of receiver dynamics, or possibly in the receiver itself, which may struggle to maintain accurate tracking at orbital velocities of approximately 7 km/s. This indicates that under alternative simulation setups, or potentially in real-world conditions, positional accuracy could be improved further.

It is noteworthy that the kinematic receivers exhibit a consistent height offset. Since this offset appears in observations from both receivers, it is likely a simulator artefact, with the *u-blox* receiver showing greater sensitivity (larger deviations).

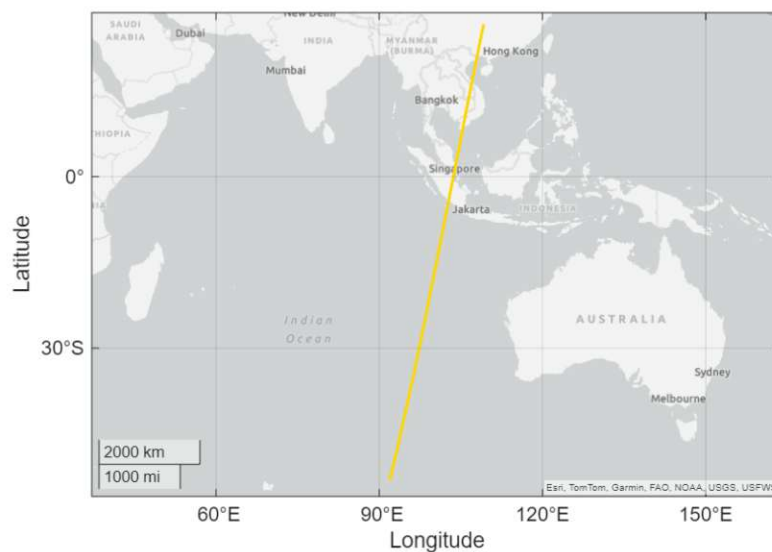


Figure 5.2: Ground track of the Astrocast CubeSat on 1 December 2022 between 05:00 and 05:20 GPS time.

For the moving receiver, the path analysis (Figure 5.2) indicates more rapid latitude changes, leading to increased positional errors in that direction, which is consistent with the results observed for both code-only and code-plus-phase solutions. In contrast, the static receiver shows slightly improved latitude accuracy in the code-plus-phase solutions, which is consistent with literature (e.g. see Savchuk et al. (2020)).

3D position errors are summarised in Table 5.1. Code-only solutions exhibit higher 3D errors than code-plus-phase solutions (mean: 2.733 m vs. 0.4 m; RMSE: 2.839 m vs. 0.462 m), consistent with the graphical results presented in Sections 4.3 and 4.4. Montenbruck et al. (2021) demonstrated that GNSS real-time navigation can achieve 10 cm 3D errors for Sentinel-6 satellites. Our results indicate that further improvements are feasible, potentially through enhancements to the simulator or the dynamic model used in the Kalman filter.

		Code			Code + Phase		
	Run	Mean [m]	σ [m]	RMSE [m]	Mean [m]	σ [m]	RMSE [m]
rakon	1	2.601	0.508	2.650	0.525	0.097	0.534
	2	3.646	0.574	3.691	0.301	0.337	0.452
	3	2.911	0.542	2.961	0.291	0.135	0.321
	all	3.053	0.697	3.131	0.372	0.242	0.444
u-blox	1	1.697	0.504	1.770	0.469	0.239	0.526
	2	2.548	0.413	2.582	0.380	0.124	0.405
	3	2.995	0.400	3.022	0.437	0.238	0.498
	all	2.414	0.696	2.512	0.428	0.214	0.479
combined		2.733	0.766	2.839	0.400	0.230	0.462

Table 5.1: 3D position error for all kinematic observations with trend removed.

6 Conclusion

6.1 Summary and Answers to Research Questions

The evaluation of commercial GNSS receivers under simulated space conditions showed that both devices were generally capable of reliable satellite tracking. Only a limited number of short data gaps occurred, and sufficient observations were available to compute continuous position solutions. As expected, performance degraded for satellites at low elevation angles, where weaker SNR and longer acquisition times were observed, and under reduced signal power levels, which caused more frequent tracking interruptions.

In terms of positioning accuracy, the results suggest that the receivers achieved acceptable performance within the tested conditions. The 3D position error of approximately 0.4 m indicates reasonable consistency but does not necessarily reflect the true in-orbit potential, as simulator-induced effects remain uncertain. It is therefore likely that actual performance in space would be better, assuming similar signal conditions. Overall, the findings support the feasibility of using low-cost commercial GNSS receivers for POD of nanosatellites, provided that receiver configurations and tracking loops are properly adapted to the dynamic environment.

Regarding data processing, the study demonstrated that the revised *raPPPid* framework (Extended Kalman filter added) can be effectively applied to nanosatellite scenarios with only moderate adjustments.

6.2 Limitations

The primary limitation of this study arises from the simulator, which introduces effects that cannot be fully characterised or verified. It appears that the simulator does not accurately reproduce highly kinematic conditions, leading to potential discrepancies in position accuracy and signal dynamics. Consequently, some of the observed deviations are likely attributable to simulator artefacts rather than receiver performance. Additionally, the receivers themselves may introduce biases, as indicated by instances where deviations between expected and measured values exhibit opposite signs for the two devices.

6.3 Outlook on Future Work

Future work should focus on identifying and mitigating the simulator-related issues to ensure realistic signal dynamics. A more comprehensive analysis including additional frequencies (e.g., L2, L5) and satellite constellations such as Galileo, GLONASS, and BeiDou would allow a broader evaluation of receiver performance in space.

List of Figures

3.1	Differences in Doppler shift between epochs for each satellite: top row shows the rakon receiver (run 1), bottom row shows the simulated observations; (a) corresponds to measurements before manual interpolation (interpolation performed by the simulator), (b) after the trajectory was interpolated manually.	11
3.2	Streaming setup.	13
3.3	In- and outputs of main processing steps.	14
3.4	Overview of default values of the extended Kalman filter in <i>raPPPid</i> .	16
3.5	Code (left) and phase (right) residuals of the u-blox receiver (run 1 after manual interpolation) processed in <i>raPPPid</i> using (a) basic and (b) optimized configurations.	17
4.1	Skyplot for the dynamic receiver along the Astrocast trajectory on December 1, 2022 between 5:00 and 5:20 GPS time. Satellites that had to be excluded in any of the observations of both receivers during optimisation of code-only and code-plus-phase processing are highlighted in red. The colour scale indicates how often a satellite was excluded across all twelve processed observation files.	19
4.2	Comparison of the number of valid observations per signal-strength level for both receivers. The simulated observations serve as reference.	20
4.3	Distribution of observation-gap durations for both receivers at different signal-strength levels. Each bar represents the number of gaps of a given duration.	22
4.4	Number of tracked satellites during the 20-minute observation period for both receivers at different signal-strength levels.	23
4.5	Delay between satellite rise and first successful tracking for both receivers and signal-strength levels.	24
4.6	Distribution of C/N_0 for both receivers. For each C/N_0 , the number of occurrences is counted.	26
4.7	Comparison of C/N_0 versus satellite elevation for <i>rakon</i> (top row) and <i>u-blox</i> (bottom row) receivers at -60 dBm (left) and -100 dBm (right).	27
4.8	Differences between simulated position and position calculated from observations in latitude, longitude, and height.	29
4.9	Differences between simulated position and position calculated from observations in latitude, longitude, and height.	31
4.10	Differences in position (latitude, longitude, height) between simulated position and calculated position with trend removed.	32
4.11	Differences between simulated position and position calculated from observations in latitude, longitude, and height.	34
4.12	Differences in position (latitude, longitude, height) between simulated position and calculated position with trend removed.	35

LIST OF FIGURES

4.13	Differences between simulated position and position calculated from observations in latitude, longitude, and height.	37
4.14	Differences in position (latitude, longitude, height) between simulated position and calculated position with trend removed.	38
5.1	Boxplot of real observed C/N_0 values on board an Astrocast CubeSat nanosatellite. Outliers are marked in red.	39
5.2	Ground track of the Astrocast CubeSat on 1 December 2022 between 05:00 and 05:20 GPS time.	40

List of Tables

3.1	Selected technical specifications of both receivers.	12
3.2	Overview of generated and processed data.	15
4.1	Calculated median time delays between satellite rise time and first tracking at -60 dBm (a) and -100 dBm (b) across all observations of both receivers. Median elevation and azimuth are calculated for the position of first tracking. The tables are sorted by elevation.	25
4.2	Noise characteristics of time-differenced GPS L1 observations (C1C, L1C, D1C) for both receivers and signal levels.	28
4.3	Residuals and optimisation parameters of the static position solution.	29
4.4	Residuals and optimisation parameters of the kinematic code measurements.	30
4.5	Residuals and optimisation parameters of static measurements using code and phase.	33
4.6	Residuals and optimisation parameters of kinematic measurements using code and phase.	36
5.1	3D position error for all kinematic observations with trend removed.	41

References

- Allahviridi-Zadeh, A., Wang, K., & El-Mowafy, A. (2022). Precise orbit determination of LEO satellites based on undifferenced GNSS observations [Publisher: American Society of Civil Engineers]. *Journal of Surveying Engineering*, 148(1), 03121001. [https://doi.org/10.1061/\(ASCE\)SU.1943-5428.0000382](https://doi.org/10.1061/(ASCE)SU.1943-5428.0000382)
- Andrews, A. P., & Grewal, M. S. (2008). *Kalman filtering: Theory and practice using MATLAB* (3rd ed.). Wiley. <https://doi.org/10.1002/9780470377819>
- Borre, K., Akos, D. M., Bertelsen, N., Rinder, P., & Jensen, S. H. (2006). *A software-defined GPS and galileo receiver*. Birkhäuser. <https://doi.org/10.1007/978-0-8176-4540-3>
- Capuano, V., Botteron, C., & Farine, P.-A. (2013). GNSS performances for MEO, GEO and HEO. *Proceedings of the International Astronautical Congress, IAC*.
- Gill, E., Morton, J., Axelrad, P., Akos, D. M., Centrella, M., & Speretta, S. (2023). Overview of space-capable global navigation satellite systems receivers: Heritage, status and the trend towards miniaturization. *Sensors*, 23(17), 7648. <https://doi.org/10.3390/s23177648>
- Glaner, M. F. (2022). *Towards instantaneous PPP convergence using multiple GNSS signals*. <https://doi.org/10.34726/hss.2022.73610>
- Glaner, M. F., & Weber, R. (2023). An open-source software package for precise point positioning: raPPPid. *GPS Solutions*, 27(4), 174. <https://doi.org/10.1007/s10291-023-01488-4>
- Hauschild, A. (2017). Basic observation equations. In P. J. Teunissen & O. Montenbruck (Eds.), *Springer handbook of global navigation satellite systems* (pp. 561–582). Springer International Publishing. https://doi.org/10.1007/978-3-319-42928-1_19
- Héroux, P., & Kouba, J. (1995). GPS precise point positioning with a difference.
- Hofmann-Wellenhof, B., Lichtenegger, H., & Collins, J. (1997). *Global positioning system: Theory and practice*. Springer Vienna. <https://doi.org/10.1007/978-3-7091-3297-5>
- Hofmann-Wellenhof, B., Lichtenegger, H., & Wasle, E. (2008). *GNSS — global navigation satellite systems*. Springer. <https://doi.org/10.1007/978-3-211-73017-1>
- Hohensinn, R., Stauffer, R., Glaner, M. F., Herrera Pinzón, I. D., Vuadens, E., Rossi, Y., Clinton, J., & Rothacher, M. (2022). Low-cost GNSS and real-time PPP: Assessing the precision of the u-blox ZED-f9p for kinematic monitoring applications. *Remote Sensing*, 14(20), 5100. <https://doi.org/10.3390/rs14205100>
- Kalman, R. E. (1960). A new approach to linear filtering and prediction problems. *ASME Journal of Basic Engineering*, 82, 35–45. <https://doi.org/10.1115/1.3662552>
- Kaplan, E. D., & Hegarty, C. J. (Eds.). (2006). *Understanding GPS: Principles and applications* (Second edition). Artech House.
- Karabatić, A. (2011). *Precise point positioning (PPP) : An alternative technique for ground based GNSS troposphere monitoring*. <https://repositum.tuwien.at/handle/20.500.12708/11254>

REFERENCES

- Malys, S., & Jensen, P. A. (1990). Geodetic point positioning with GPS carrier beat phase data from the CASA UNO experiment. *Geophysical Research Letters*, 17(5), 651–654. <https://doi.org/10.1029/GL017i005p00651>
- Mao, X., Arnold, D., Kalarus, M., Padovan, S., & Jäggi, A. (2023). GNSS-based precise orbit determination for maneuvering LEO satellites. *GPS Solutions*, 27(3), 147. <https://doi.org/10.1007/s10291-023-01494-6>
- Montenbruck, O., Kunzi, F., De Oliveira Salgueiro, F., Gini, F., & Cordero Limón, M. (2025). GNSS-based synchronization and monitoring of LEO-PNT onboard time. *Advances in Space Research*, 76(11), 7144–7159. <https://doi.org/10.1016/j.asr.2025.09.047>
- Montenbruck, O., Kunzi, F., & Hauschild, A. (2021). Performance assessment of GNSS-based real-time navigation for the sentinel-6 spacecraft. *GPS Solutions*, 26(1), 12. <https://doi.org/10.1007/s10291-021-01198-9>
- Müller, L., Chen, K., Möller, G., Rothacher, M., Soja, B., & Lopez, L. (2024). Real-time navigation solutions of low-cost off-the-shelf GNSS receivers on board the astrocast constellation satellites. *Advances in Space Research*, 73(1), 2–19. <https://doi.org/10.1016/j.asr.2023.10.001>
- Pratap, M., & Per, E. (2006). *Global positioning system: Signals, measurements, and performance* (2nd ed.). Ganga-Jamuna Press.
- Savchuk, S., Cwiklak, J., & Khoptar, A. (2020). Precise point positioning technique versus relative positioning. *Baltic Surveying*, 12, 39–43. <https://doi.org/10.22616/j.balticsurveying.2020.006>
- Teunissen, P. (2020). GNSS precise point positioning. In *Position, navigation, and timing technologies in the 21st century* (pp. 503–528). John Wiley & Sons, Ltd. <https://doi.org/10.1002/9781119458449.ch20>
- Verhagen, S., & Teunissen, P. (2017). Least-squares estimation and kalman filtering. In P. Teunissen & O. Montenbruck (Eds.), *Springer handbook of global navigation satellite systems*. Springer. https://doi.org/10.1007/978-3-319-42928-1_22
- Wu, J. T., Wu, S. C., Hajj, G. A., Bertiger, W. I., & Lichten, S. M. (1993). Effects of antenna orientation on GPS carrier phase. *manuscripta geodaetica*, 18(2), 91–98. <https://doi.org/10.1007/BF03655303>
- Yao, Z., & Lu, M. (2021). *Next-generation GNSS signal design: Theories, principles and technologies* (1st ed.). Springer Singapore. <https://doi.org/10.1007/978-981-15-5799-6>
- Zumberge, J. F., Heflin, M. B., Jefferson, D. C., Watkins, M. M., & Webb, F. H. (1997). Precise point positioning for the efficient and robust analysis of GPS data from large networks. *Journal of Geophysical Research: Solid Earth*, 102, 5005–5017. <https://doi.org/10.1029/96JB03860>